Exchange currents in nucleon electroexcitation

U. Meyer,[1,*] E. Hernández,[2,†] and A. J. Buchmann[1,‡]
[1]*Institute for Theoretical Physics, University of Tübingen, Auf der Morgenstelle 14, D-72076 Tübingen, Germany*
[2]*Grupo de Fisica Nuclear, Universidad de Salamanca, E-37008 Salamanca, Spain*
(Received 19 March 2001; published 16 August 2001)

We calculate the scalar and transverse helicity amplitudes for the electromagnetic excitation of nucleon resonances as a function of the photon four-momentum transfer. The helicity amplitudes are decomposed into electromagnetic multipoles and connected to the $\gamma N \rightarrow N^*$ transition form factors. The internal N and N^* dynamics is described by a constituent quark model (CQM) Hamiltonian with gluon, pion, and σ-meson exchange potentials as residual interactions. The N and N^*-resonance wave functions are obtained by solving the Schrödinger equation in a harmonic oscillator basis which contains up to $N=2$ excitation quanta. For the electromagnetic current we include, in addition to the one-body current, two-body exchange currents associated with the quark-quark potentials. Exchange currents provide an effective description of the cloud of $q\bar{q}$ pairs, which together with the valence quarks are important degrees of freedom in physical hadrons. We obtain sizable contributions of the two-body exchange currents for nearly all γNN^* amplitudes. For some observables, e.g., the $C2/M1$ ratio in the $\gamma N \rightarrow \Delta(1232)$ transition, and the $M1$ transition to the $N^*(1440)$, exchange currents provide the most important contribution.

DOI: 10.1103/PhysRevC.64.035203 PACS number(s): 12.39.Jh, 13.40.Em, 13.40.Hq, 14.20.Gk

I. INTRODUCTION

Several continuous electron beam accelerator facilities and high energy photon sources are currently used to study the inner structure of the nucleon (N) and its excited states (N^*) with higher precision. From the cross sections for electromagnetic pionproduction with real or virtual photons $\gamma + N \rightarrow N^* \rightarrow N + \pi$, the scalar and transverse helicity amplitudes (see Fig. 1) for nucleon resonance production can be extracted and compared with theory [1]. The electromagnetic pionproduction data are complementary to pion-nucleon scattering experiments, such as $\pi + N \rightarrow N^* \rightarrow N + \pi$, which revealed the existence of a rich spectrum of excited nucleon states. However, knowledge of the N^* masses alone does not allow to discriminate between models. Rather different models of nucleon structure lead to nearly the same spectrum of excited states.

Using the electron as a probe, further details of nucleon structure can be explored. Because the e.m. interaction is well known, and because the electron is pointlike, the measured cross sections are directly related to the structure of the proton. With the help of polarization and coincidence experiments, the contribution of individual electromagnetic multipoles to the e.m. $\gamma + N \rightarrow N^*$ helicity amplitudes can be isolated. The e.m. multipoles carry information about the geometrical shape of the N and N^* and the degrees of freedom that are being excited. In electron scattering, the helicity amplitudes are measured at different photon four-momentum transfers, and the internal N and N^* structure can be mapped out from small to large distances. It is hoped that these experiments together with theoretical efforts will eventually lead to a comprehensive understanding of the inner composition of the nucleon and the dynamics of its quark-gluon constituents.

Photon induced reactions on the nucleon were already studied in the 1960s and 1970s. At that time, most data were taken at the real photon point, for which the energy transfer ω is equal to the three-momentum transfer $\mathbf{q}$, i.e., at four-momentum transfer $Q^2 = -q_\mu^2 = \omega^2 - \mathbf{q}^2 = 0$. On the theory side, a nonrelativistic quark model (NRQM) was used to analyze and interpret the data [2–4]. In these investigations a harmonic oscillator (h.o.) basis for the baryon wave functions (usually a single Gaussian) was used. Furthermore,

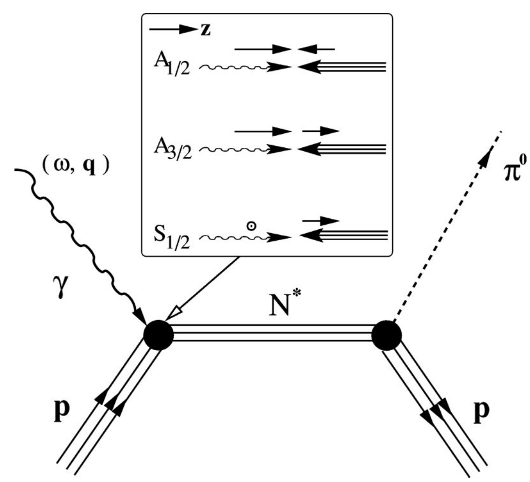

FIG. 1. Electroproduction of pions on the nucleon in the γN center of mass system. A virtual photon (γ) with energy transfer ω, three-momentum transfer $\mathbf{q} = q\mathbf{e}_z$, and spin projection 1 or 0 hits a proton and produces an excited nucleon state N^*, which strongly decays, e.g., into a proton and π^0. The γNN^* vertex is described by the transversal A_λ and scalar S_λ helicity amplitudes. The index denotes the total spin projection of the incoming γ and N which is equal to the spin projection of the N^* resonance.

*Email address: Ulrich.Meyer@deutsche-boerse.com
†Email address: gajatee@gugu.usal.es
‡Email address: alfons.buchmann@uni-tuebingen.de

one-body quark currents were assumed to provide the main mechanism for the electromagnetic excitation of these resonances (single quark transition model). Although the single quark transition model describes the photocouplings of many resonances quite well, for some resonances, e.g., the $\Delta(1232)$, the $N^*(1440)$, and the negative parity resonance $N^*(1535)$ large discrepancies between theory and experiment remained. In addition, the single quark transition model employed inconsistent nucleon size parameters in various applications. For example, in order to describe the experimental nucleon spectrum and the empirical helicity amplitudes for the $\gamma N \rightarrow N^*(1535)$ transition small quark core radius $b \approx 0.5$ fm was necessary, whereas the experimental proton and neutron charge radii demanded a value of $b \approx 1$ fm [5].

One has tried to solve these problems by including relativistic corrections in the one-body current and in the wave functions [6–9]. Relativistic corrections to the single quark current helped to increase the proton charge radius, but the neutron charge radius r_n^2 and the $N \rightarrow \Delta$ quadrupole moment $Q_{p\rightarrow\Delta^+}$ were still much too small compared to experiment [10]. These investigations showed that some important degrees of freedom were still missing in the single quark transition model.

Thus, also in these improved versions of the NRQM several problems remain. For example, almost all quark models underpredict the magnetic dipole transition strength to the $\Delta(1232)$. At the real photon point, the calculated transition magnetic moment

$$\mu_{p\rightarrow\Delta^+} = -\sqrt{2}\mu_n \tag{1}$$

is some 30–40 % lower than experiment [11]. This discrepancy exists since the early days of the quark model [12].

Another problem is the simultaneous description of the $A_{1/2}$ amplitude for the $P_{11}(1440)$ excitation at the real photon point, where it is large, and for finite momentum transfers where it is very small. For real photons, the $A_{1/2}$ amplitude calculated with one-body currents is three times smaller than the experimental value. This holds for both the proton and neutron. Addition of relativistic corrections to the single quark current did not improve matters in this case [9]. In contrast to the underestimation of the experimental photocouplings, most quark models overestimate the $A_{1/2}$ and $S_{1/2}$ amplitudes at finite momentum transfers. There, the experimental helicity amplitude is nearly zero. This phenomenon, called electroquenching, cannot be reproduced in most quark models [1]. At present, the experimental transverse and scalar helicity amplitudes to the Roper are described best in the approach of Li *et al.* [13]. These authors assume that the Roper is not a pure three-quark resonance, but that its wave function contains an admixture of a three-quark/constituent gluon configuration ($|\mathbf{qqqg}\rangle$).

Our way has been to include two-body exchange currents [14–21] in order to improve the single quark transition model. Exchange currents are necessary in order to satisfy the continuity equation for the electromagnetic current if the quarks interact via momentum-dependent and/or isospin-dependent interactions. In more physical terms, the exchange currents effectively account for the cloud of $q\bar{q}$ pairs surrounding the valence quark core. Several years ago we found that the neutron charge form factor and the $N \rightarrow \Delta$ quadrupole transition form factor are mainly governed by the two-body exchange currents. Using a small quark core radius $b \approx 0.6$ fm consistent with the excited nucleon spectrum, a good agreement with the experimental neutron charge radius and the $N \rightarrow \Delta$ transition quadrupole moment has been obtained [14,15]. Furthermore, we found that these observables are closely related and derived a parameter-independent relation between them [15]

$$Q_{p\rightarrow\Delta^+} = \frac{1}{\sqrt{2}} r_n^2. \tag{2}$$

This is in good agreement with the value extracted from the pion production data [22–25].

Similarly, for the photoproduction of the $P_{11}(1440)$ and $S_{11}(1535)$ resonances, the inclusion of exchange currents leads to a better agreement with the data [16]. In a first step we used unmixed harmonic oscillator (h.o.) wave functions in the evaluation of the exchange current contribution.

In the present work, we generalize our previous calculation to electron induced N^* excitation, and investigate the dependence of the helicity amplitudes on the photon four-momentum transfer Q^2. Furthermore, we enlarge the Hilbert space and expand baryon wave functions in terms of h.o. eigenstates up to $N=2$ harmonic oscillator quanta. The nucleon is then a superposition of five different h.o. states (configuration mixing). In addition, we study the effect of exchange currents and of configuration mixing (CM) on the $C2/M1$ and $E2/M1$ ratios for Δ electroexcitation, and other observables. We will show that exchange currents give important contributions to nearly all observables.

The paper is divided in five parts. In Sec. II, we present the chiral quark model (χQM) used to calculate the baryon wave functions, and the electromagnetic one- and two-body currents. In Sec. III we present our results and compare them with the experimental data and with the results obtained by other authors. In Sec. IV, we summarize our findings and give an outlook to future research. The formulas connecting the e.m. helicity amplitudes and the electromagnetic multipole form factors are listed in an Appendix.

II. THE CHIRAL QUARK MODEL

A. The Hamiltonian

The chiral quark model (χQM) was devised to effectively describe the low-energy properties of quantum chromodynamics (QCD). As a consequence of the spontaneous breakdown of chiral symmetry of QCD at the 1 GeV scale, the nearly massless quarks in the QCD Lagrangian transform into massive quasiparticles called constituent quarks. A constituent quark is an extended quasiparticle with finite hadronic and e.m. size, a mass of about 1/3 of the nucleon mass, and strong effective interactions. The spontaneous chiral symmetry breaking leads to the appearance of an octet of pseudoscalar Goldstone bosons (GB) and their scalar chiral partners, which couple to the constituent quarks. This is in

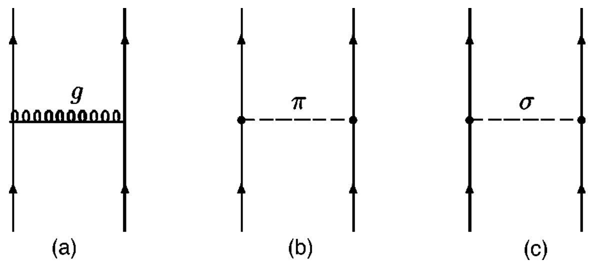

FIG. 2. Residual (a) one-gluon, (b) one-pion, and (c) one-sigma exchange potentials between constituent quarks. The hadronic size r_q of the constituent quarks is indicated by small dots.

contrast to the elementary particle picture of quarks and gluons at high energies. There, pointlike (current) quarks with masses $m_c \approx 5$–10 MeV interact rather weakly via one-gluon exchange, and perturbative QCD can be used to make quantitative predictions.

The χQM Hamiltonian contains besides the confinement interaction (V^c), two-body potentials originating from one-pion (V^π),[1] one-sigma (V^σ) and from one-gluon (V^g) exchange:

$$H=\sum_{i=1}^{3}\left(m_q+\frac{\mathbf{p}_i^2}{2m_q}\right)-\frac{\mathbf{P}^2}{6m_q}+\sum_{i<j=1}^{3}[V^c(\mathbf{r}_i,\mathbf{r}_j)+V^\pi(\mathbf{r}_i,\mathbf{r}_j)+V^\sigma(\mathbf{r}_i,\mathbf{r}_j)+V^g(\mathbf{r}_i,\mathbf{r}_j)], \tag{3}$$

where $\mathbf{r}_i$ and $\mathbf{p}_i$ are the position and momentum of the coordinates of the ith quark. The center of mass momentum $\mathbf{P}$ of the nucleon is subtracted so that the calculated baryon masses contain only the internal kinetic energy. Apart from the confinement interaction, the other potential terms are obtained from the Feynman diagrams in Fig. 2.

We use the following spin-dependent quark-quark potentials in the calculations of the baryon wave functions:

$$V^\pi(|\mathbf{r}_i-\mathbf{r}_j|)=\frac{g_{\pi q}^2}{4\pi}\frac{\Lambda_\pi^2}{\Lambda_\pi^2-m_\pi^2}\frac{\boldsymbol{\tau}_i\cdot\boldsymbol{\tau}_j}{4m_q^2}\boldsymbol{\sigma}_i\cdot\boldsymbol{\nabla}_r\boldsymbol{\sigma}_j\cdot\boldsymbol{\nabla}_r\left(\frac{e^{-m_\pi r}}{r}-\frac{e^{-\Lambda_\pi r}}{r}\right), \tag{4}$$

$$V^\sigma(|\mathbf{r}_i-\mathbf{r}_j|)=-\frac{g_{\sigma q}^2}{4\pi}\frac{\Lambda_\sigma^2}{\Lambda_\sigma^2-m_\sigma^2}\left(\frac{e^{-m_\sigma r}}{r}-\frac{e^{-\Lambda_\sigma r}}{r}\right), \tag{5}$$

$$V^g(|\mathbf{r}_i-\mathbf{r}_j|)=\frac{\alpha_s}{4}\boldsymbol{\lambda}_i\cdot\boldsymbol{\lambda}_j\left\{\frac{1}{r}-\frac{\pi}{m_q^2}\left(1+\frac{2}{3}\boldsymbol{\sigma}_i\cdot\boldsymbol{\sigma}_j\right)\delta(\mathbf{r})-\frac{1}{4m_q^2}(3\boldsymbol{\sigma}_i\cdot\hat{\mathbf{r}}\boldsymbol{\sigma}_j\cdot\hat{\mathbf{r}}-\boldsymbol{\sigma}_i\cdot\boldsymbol{\sigma}_j)\frac{1}{r^3}\right\}, \tag{6}$$

with $r=|\mathbf{r}_i-\mathbf{r}_j|$. Here, $\boldsymbol{\tau}_i$ are the $SU(2)_{\mathrm{isospin}}$ Pauli matrices, $\boldsymbol{\lambda}_i$ are the $SU(3)_{\mathrm{color}}$ Gell-Mann matrices, m_q is the constituent quark mass, m_π is the pion mass, and m_σ the σ meson mass. For the pion and σ meson exchange potentials, we describe the extended quark-meson vertices by a form factor

$$F(\mathbf{k}^2)=\left(\frac{\Lambda^2}{\Lambda^2+\mathbf{k}^2}\right)^{1/2}. \tag{7}$$

Here, $\mathbf{k}$ is the three-momentum of the exchanged meson and Λ is the cutoff parameter. In coordinate space this leads to a second Yukawa term with a fictitious meson mass Λ.

In the meson exchange potentials the quark-meson couplings ($g_{\pi q}, g_{\sigma q}$), the cutoff parameters Λ, as well as the meson and quark masses are related via the chiral symmetry constraints [26,27]:

$$\frac{g_{\sigma q}^2}{4\pi}=\frac{g_{\pi q}^2}{4\pi},\qquad \Lambda_\sigma=\Lambda_\pi,\qquad m_\sigma^2=4m_q^2+m_\pi^2. \tag{8}$$

Unlike nuclear physics where the σ mass and the σN coupling strength are fitted to experimental nucleon-nucleon scattering data, the σ parameters of the χQM are fixed by the empirical pion mass and the pion-quark coupling $g_{\pi q}$. The latter is determined by the experimental πN coupling strength $f_{\pi N}^2/4\pi=0.0749$ via

$$\frac{g_{\pi q}^2}{4\pi}=\left(\frac{3}{5}\right)^2\frac{f_{\pi N}^2}{4\pi}\left(\frac{2m_q}{m_\pi}\right)^2. \tag{9}$$

We also include the one-gluon exchange potential V^g as an effective description of the short-range quark-gluon dynamics. The one-gluon exchange potential was introduced by de Rújula *et al.* [28], and later successfully used to explain certain regularities in the spectrum of excited baryon states [29]. In V^g, α_s is the effective quark-gluon coupling constant (independent of the gluon momentum transfer). This parameter is determined from the experimental $N-\Delta$ mass splitting.

Recently, the baryon mass spectrum has been described by GB octet exchange alone without a gluon-exchange interaction [30]. However, we found it difficult to attribute all of the $N-\Delta$ mass splitting to one-pion exchange without stretching some of the parameters beyond what is physically meaningful. For example, if one wants to attribute all of the $N-\Delta$ mass splitting to one-pion exchange, one must make the quark core radius of the nucleon smaller than 0.4 fm (see Fig. 2 in Ref. [14]) in which case it is nearly impossible to describe the electromagnetic form factors of the nucleon [31]. Furthermore, including an effective one-gluon exchange potential has certain conceptual advantages compared to a pure Goldstone boson exchange picture [32]. The former has the same spin-color symmetry as QCD, and predicts a continuous increase of the hyperfine splittings between vector and pseudoscalar mesons when going from

[1]Because we study the nucleon and Δ sector, we neglect the strange mesons of the pseudoscalar nonet octet. From the nonstrange mesons we only include the pion and its chiral partner, the σ meson. We do not include the η. Its contribution to various observables is suppressed because of its larger mass [17].

TABLE I. Quark model parameters. Set I: for quadratic confinement and unmixed wave functions. Set II: for exponential confinement and configuration mixed wave functions. The constituent quark mass is denoted by m_q, b is the harmonic oscillator constant, α_S is the quark-gluon coupling strength, a is the confinement strength, μ the color screening length, C a constant term in the confinement potential, and Λ is the cutoff in the meson exchange potentials.

	m_q (MeV)	b (fm)	α_S	a	μ (fm^{-1})	C (MeV)	Λ (fm^{-1})
Set I (quad. conf.)	313	0.613	1.093	20.20 (MeV/fm^2)			4.2
Set II (exp. conf.)	313	0.695	0.978	447.443 (MeV)	2.0	-913.741	4.2

heavy to light quark flavors in agreement with experiment [33]. In addition, the color factor in the color-magnetic spin-spin interaction of QCD explains why the π-ρ splitting is nearly twice the N-Δ splitting. A pure Goldstone boson exchange model does not provide such connections.

The constituent quarks in the nucleon are confined by a long-range, spin-independent, scalar two-body potential. For convenience a harmonic oscillator potential is often taken

$$V^c(|\mathbf{r}_i-\mathbf{r}_j|)=-a\boldsymbol{\lambda}_i\cdot\boldsymbol{\lambda}_j(\mathbf{r}_i-\mathbf{r}_j)^2. \tag{10}$$

In order to facilitate a comparison with our previous results with a harmonic oscillator confinement potential [16], we evaluate the matrix elements of the Hamiltonian and e.m. current for unmixed wave functions with our standard set of parameters (set I in Table I) based on Eq. (10).

However, from lattice calculations we know that a linear radial function is more realistic. A linear confinement, which at larger distances is screened by quark-antiquark pair creation is found in some lattice calculations. The effect of these color screening confinement potentials on the baryon spectrum has recently been investigated [34]. Here, we consider a color screening potential of the form

$$V^c(|\mathbf{r}_i-\mathbf{r}_j|)=-a\boldsymbol{\lambda}_i\cdot\boldsymbol{\lambda}_j(1-e^{-\mu r})+C, \tag{11}$$

and a corresponding set of parameters (set II in Table I) for mixed wave functions. In contrast to the standard h.o. confinement, the color-screened confinement potential of Eq. (11) is very strong. For small r it grows linearly with r, and its strength is about 1 GeV/fm. This corresponds to the phenomenological (universal) string tension needed to explain the Regge trajectories of excited meson and baryon states.

Spin-orbit potentials arising from the confinement potential the residual gluon and sigma interactions in Fig. 2 are not included for the calculation of the masses and mixing parameters.

In summary, the chiral quark potential model provides an effective description of low-energy baryon properties. It describes the symmetries and dynamics of the underlying field theory of QCD including important low-energy dynamical features, such as spontaneous chiral symmetry breaking.

B. The baryon wave functions

As usual, the radial three-quark wave function of the baryon is expanded in the harmonic oscillator basis. In a previous study [16] we used unmixed wave functions where all three quarks remain in their lowest h.o. state $|S_S\rangle$. The ground state baryon wave function is an inner product of the orbital, spin-isospin, and color wave functions and given by

$$|^{2(4)}S_S\rangle_{N(\Delta)}=(1/\sqrt{3}\pi b^2)^{3/2}\exp(-(\boldsymbol{\rho}^2/4b^2 +\boldsymbol{\lambda}^2/3b^2))|ST\rangle^{N(\Delta)}\times|[111]\rangle^{N(\Delta)}_{\text{color}}, \tag{12}$$

where the Jacobi coordinates $\boldsymbol{\rho}$ and $\boldsymbol{\lambda}$ are defined as $\boldsymbol{\rho}=\mathbf{r}_1-\mathbf{r}_2$ and $\boldsymbol{\lambda}=\mathbf{r}_3-(\mathbf{r}_1+\mathbf{r}_2)/2$. Here, b is the harmonic oscillator parameter also referred to as quark core radius. The spin-isospin wave function is denoted by $|ST\rangle$, and the completely antisymmetric color wave function by $|[111]\rangle_{\text{color}}$.

In the case of unmixed wave functions, we follow the procedure described in Ref. [15], where the parameters are chosen in such a way that the experimental nucleon and Δ masses are reproduced, and the so-called stability condition

$$\frac{\partial M_N}{\partial b}=0 \tag{13}$$

is satisfied. We then obtain the parameters of set I given in Table I.

In this paper, we go beyond this approximation, and expand the baryon wave functions in a larger h.o. basis including up to $N=2$ excitation quanta. For the negative parity sector we continue to use unmixed wave functions because the calculated mixing coefficients are small with the present confinement potential. With configuration mixing, the $N(939)$ and $N^*(1440)$ wave functions are superpositions of five h.o. states, while the $\Delta(1232)$ is a superposition of four h.o. states:

$$\begin{aligned}|N\rangle&=a_{S_S}|^2S_S\rangle+a_{S_{S'}}|^2S_{S'}\rangle+a_{S_M}|^2S_M\rangle+a_{D_M}|^4D_M\rangle\\&\quad+a_{P_A}|^2P_A\rangle,\\|\Delta\rangle&=b_{S_S}|^4S_S\rangle+b_{S_{S'}}|^4S_{S'}\rangle+b_{D_S}|^4D_S\rangle+b_{D_M}|^2D_M\rangle.\end{aligned} \tag{14}$$

For the h.o. states we follow the notation $|^{2S+1}L_{\text{sym}}\rangle$ with S being the total spin, and L the total orbital angular momentum. The amplitudes a and b are determined by diagonalization of the Hamiltonian of Eq. (3) in this restricted h.o. basis. The results are given in Table II. The Roper is dominated by a radial excitation of the $N(939)$ ground state wave function, the so-called "breathing mode." The mixing with the P-wave is for both the nucleon and its resonances about two orders of magnitude smaller than the D-wave amplitudes.

TABLE II. Admixture coefficients in the wave function of Eq. (14) calculated with the Hamiltonian of Eq. (3) and parameter set II in an $N=2$ harmonic oscillator wave function space.

Set II	a_{S_S}	$a_{S'_S}$	a_{S_M}	a_{D_M}	a_{P_A}
$P_{11}(939)$	0.898	-0.408	-0.161	-0.0120	0.0002
$P_{11}(1440)$	0.381	0.907	-0.178	0.0098	0.0004
Set II	b_{S_S}	$b_{S_{S'}}$	b_{D_S}	b_{D_M}	
$P_{33}(1232)$	0.983	-0.143	-0.0981	0.0662	

Therefore we neglect the P-wave contribution in the calculation of the e.m. helicity amplitudes.

The baryon mass spectrum alone does not provide sufficient constraints in order to find the best overall fit and to fix the parameter set uniquely. For that reason we studied the e.m. nucleon form factors. Parameter set II of Table I gives a reasonable fit to the experimental baryon mass spectrum and the nucleon e.m. properties. The masses of some selected nucleon resonances are listed in Table III. The calculated e.m. properties of the nucleon ground state are similar to those calculated in Ref. [14].

C. The electromagnetic current

In order to calculate photon induced reactions on the nucleon we have to know its e.m. four-vector current J_μ. In first order perturbation theory the transition matrix elements of the photon-nucleon current interaction have to be calculated. The e.m. interaction Hamiltonian is given by

$$H_{\gamma N}=\int d^4x J_\mu(x)A^\mu(x), \tag{15}$$

with $A_\mu(x)=[\phi(x),-\mathbf{A}(x)]$ being the photon field. The nucleon e.m. current density $J_\mu(x)=[\rho(x),-\mathbf{J}(x)]$ is expressed in terms of quark degrees of freedom. In most investigations only the one-body terms[2] (impulse approximation) of the e.m. current

$$\rho_{[1]}(\mathbf{q})=\sum_{i=1}^{3} e_i e^{i\mathbf{q}\cdot\mathbf{r}_i},$$
$$\mathbf{J}_{[1]}(\mathbf{q})=\sum_{i=1}^{3}\frac{e_i}{2m_q}\left(i[\boldsymbol{\sigma}_i\times\mathbf{p}_i,e^{i\mathbf{q}\cdot\mathbf{r}_i}]+\{\mathbf{p}_i,e^{i\mathbf{q}\cdot\mathbf{r}_i}\}\right) \tag{16}$$

have been considered, where the sum over i indicates the particle number of the three valence quarks, and $\mathbf{q}$ is the photon three-momentum. Here, the quark charge e_i is given as $e_i=e(1+3\boldsymbol{\tau}_{3\,i})/6$. The first term in $\mathbf{J}_{[1]}$ is called spin current and the second term convection current. In impulse approximation, quark dynamics is neglected in the current operator, i.e., a single quark absorbs the entire photon four-momentum while the other two quarks are not affected. This approximation is often referred to as the single quark transition model.

It is well known that in a system of interacting quarks the usual approximation $\mathbf{J}\approx\mathbf{J}_{[1]}$ violates the continuity equation for the e.m. current. In order to satisfy the continuity equation in the presence of interactions between the quarks, it is necessary to include the two-body exchange currents $\mathbf{J}_{[2]}$ associated with the various quark-quark potentials $V_{[2]}$ in the Hamiltonian. The total charge and current density is then a sum of one- and two-body terms

$$\rho=\rho_{[1]}+\rho_{[2]},\quad \mathbf{J}=\mathbf{J}_{[1]}+\mathbf{J}_{[2]}. \tag{17}$$

In principle one could also include three-body currents. We do not consider them in this work. Compared to the two-body currents, their contribution is suppressed by at least a

[2]The one-body nature of these operators is indicated by the subscript [1].

TABLE III. Contributions of the rest mass, kinetic energy, and the two-body interactions to the masses of the nucleon and its low-lying excited N^* resonances. The parameter set II from Table I is used. All entries are in MeV. The spectroscopic notation $L_{2I\,2J}$ for the pion nucleon partial scattering waves is used to label these resonances.

Resonance	$3m_q$	T^{kin}	V^c	V^g	V^π	V^σ	Total	Exp. [11]
$P_{11}(939)$	939	599	106	-502	-146	-58	939	939
$P_{11}(1440)$	939	453	516	-306	-47	-21	1533	$1430-1470$
$P_{33}(1232)$	939	458	206	-298	-26	-47	1232	$1230-1234$
$S_{11}(1535)$	939	515	415	-363	-33	-26	1447	$1520-1555$
$D_{13}(1520)$	939	515	415	-355	-41	-26	1447	$1515-1530$

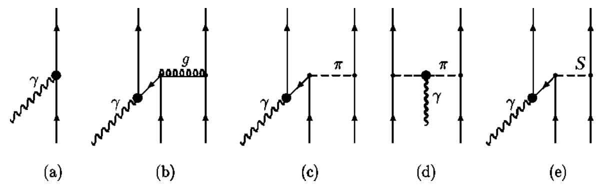

FIG. 3. Feynman diagrams for the electromagnetic current $J^{\mu}=(\rho,\mathbf{J})$: (a) one-body current; (b) gluon $q\bar{q}$ pair; (c) pion $q\bar{q}$ pair; (d) pion-in-flight; (e) scalar $q\bar{q}$ pair, i.e., σ meson or confinement exchange currents. The finite e.m. size of the constituent quarks and the pion is denoted by the large black dots.

factor 1/3. This has recently been shown for the $\rho_{[3]}$ contribution to the N and Δ charge radii in two different approaches [35,36].

We obtain the two-body exchange currents by an explicit calculation of the Feynman diagrams displayed in Figs. 3(b)–3(e). In this way we simultaneously obtain the time and spatial components of the four-vector exchange current J^{μ}. The spatial exchange currents due to gluon ($\mathbf{J}_{[2]}^{gq\bar{q}}$), pion ($\mathbf{J}_{[2]}^{\pi q\bar{q}}$, $\mathbf{J}_{[2]}^{\gamma\pi\pi}$), and scalar ($\mathbf{J}_{[2]}^{Sq\bar{q}}$) exchange interactions are given by

$$\mathbf{J}_{[2]}^{gq\bar{q}}(\mathbf{r}_i,\mathbf{r}_j,\mathbf{q}) =-\frac{\alpha_s}{4m_q^2}\boldsymbol{\lambda}_i\cdot\boldsymbol{\lambda}_j\left\{e_i e^{i\mathbf{q}\cdot\mathbf{r}_i}\frac{1}{2}(\boldsymbol{\sigma}_i+\boldsymbol{\sigma}_j)\times\mathbf{r}+(i\leftrightarrow j)\right\}\frac{1}{r^3}, \tag{18}$$

$$\mathbf{J}_{[2]}^{\pi q\bar{q}}(\mathbf{r}_i,\mathbf{r}_j,\mathbf{q})=\frac{ef_{\pi q}^2}{4\pi m_\pi^2}\{(\boldsymbol{\tau}_i\times\boldsymbol{\tau}_j)_3 e^{i\mathbf{q}\cdot\mathbf{r}_i}\boldsymbol{\sigma}_i(\boldsymbol{\sigma}_j\cdot\boldsymbol{\nabla}_r) +(i\leftrightarrow j)\}\frac{\Lambda_\pi^2}{\Lambda_\pi^2-m_\pi^2}\left(\frac{e^{-m_\pi r}}{r}-\frac{e^{-\Lambda_\pi r}}{r}\right),$$

$$\mathbf{J}_{[2]}^{\gamma\pi\pi}(\mathbf{r}_i,\mathbf{r}_j,\mathbf{q})=\frac{ef_{\pi q}^2}{4\pi m_\pi^2}(\boldsymbol{\tau}_i\times\boldsymbol{\tau}_j)_3(\boldsymbol{\sigma}_i\cdot\boldsymbol{\nabla}_i)\times(\boldsymbol{\sigma}_j\cdot\boldsymbol{\nabla}_j)\frac{\Lambda_\pi^2}{\Lambda_\pi^2-m_\pi^2}\int_{-1/2}^{+1/2}dv\,e^{i\mathbf{q}\cdot(\mathbf{R}-v\mathbf{r})}\times\left[\mathbf{z}_{m_\pi}\frac{e^{-L_{m_\pi}r}}{L_{m_\pi}r}-\mathbf{z}_{\Lambda_\pi}\frac{e^{-L_{\Lambda_\pi}r}}{L_{\Lambda_\pi}r}\right], \tag{19}$$

$$\mathbf{J}_{[2]}^{Sq\bar{q}}(\mathbf{r}_i,\mathbf{r}_j,\mathbf{q})=-\frac{i}{2m_q^2}e_i e^{i\mathbf{q}\cdot\mathbf{r}_i}V^S i\boldsymbol{\sigma}_i\times\mathbf{q}+(i\leftrightarrow j). \tag{20}$$

In the pion-in-flight exchange current, where the photon interacts directly with the exchanged pion, we use the following abbreviations $\mathbf{R}=(\mathbf{r}_i+\mathbf{r}_j)/2$ and $\mathbf{z}_m(\mathbf{q},\mathbf{r})=L_m\mathbf{r}+ivr\mathbf{q}$, where $L_m=\sqrt{\frac{1}{4}q^2(1-4v^2)+m^2}$. In the scalar exchange current, V^S stands for V^c and V^{σ}. The total two-body current of the χQM is then given by

$$\mathbf{J}_{[2]}=\mathbf{J}_{[2]}^{gq\bar{q}}+\mathbf{J}_{[2]}^{\pi q\bar{q}}+\mathbf{J}_{[2]}^{\gamma\pi\pi}+\mathbf{J}_{[2]}^{\sigma q\bar{q}}+\mathbf{J}_{[2]}^{cq\bar{q}}. \tag{21}$$

The two-body exchange charge densities corresponding to the Feynman diagrams of Figs. 3(b)–3(e) are

$$\rho_{[2]}^{gq\bar{q}}(\mathbf{r}_i,\mathbf{r}_j,\mathbf{q})=-\frac{i\alpha_s}{16m_q^3}\boldsymbol{\lambda}_i\cdot\boldsymbol{\lambda}_j\{e_i e^{i\mathbf{q}\cdot\mathbf{r}_i}(\mathbf{q}\cdot\mathbf{r}+(\boldsymbol{\sigma}_i\times\mathbf{q})\cdot(\boldsymbol{\sigma}_j\times\mathbf{r}))+(i\leftrightarrow j)\}\frac{1}{r^3}, \tag{22}$$

$$\rho_{[2]}^{\pi q\bar{q}}(\mathbf{r}_i,\mathbf{r}_j,\mathbf{q})=\frac{ie}{6}\frac{f_{\pi q}^2}{4\pi}\frac{1}{m_q m_\pi^2}(\boldsymbol{\tau}_i\cdot\boldsymbol{\tau}_j+3\tau_3^j)\times\{e^{i\mathbf{q}\cdot\mathbf{r}_i}\boldsymbol{\sigma}_i\cdot\mathbf{q}\boldsymbol{\sigma}_j\cdot\boldsymbol{\nabla}_r+(i\leftrightarrow j)\}\times\frac{\Lambda_\pi^2}{\Lambda_\pi^2-m_\pi^2}\left(\frac{e^{-m_\pi r}}{r}-\frac{e^{-\Lambda_\pi r}}{r}\right), \tag{23}$$

$$\rho_{[2]}^{\gamma\pi\pi}(\mathbf{r}_i,\mathbf{r}_j,\mathbf{q})\approx 0, \tag{24}$$

$$\rho_{[2]}^{Sq\bar{q}}(\mathbf{r}_i,\mathbf{r}_j,\mathbf{q})=\frac{1}{4m_q^3}e_i e^{i\mathbf{q}\cdot\mathbf{r}_i}\mathbf{q}^2V^S+(i\leftrightarrow j). \tag{25}$$

In lowest order in the nonrelativistic expansion there is no contribution of the pion-in-flight diagram in Fig. 3(d) to the charge density. In contrast to our previous work [14,15] the scalar exchange charge operator is in its $\mathbf{q}$ part by a factor 4/3 larger, and does not contain any gradient terms. The total two-body charge density is then

$$\rho_{[2]}=\rho_{[2]}^{gq\bar{q}}+\rho_{[2]}^{\pi q\bar{q}}+\rho_{[2]}^{\sigma q\bar{q}}+\rho_{[2]}^{cq\bar{q}}. \tag{26}$$

All two-body charge operators vanish in the limit $\mathbf{q}\to 0$. Therefore, they do not modify the total charge of the baryon.

In order to take the finite e.m. size of the constituent quarks into account, all charge and current operators in this section are multiplied with a single electromagnetic monopole form factor as given by the vector dominance model applied to constituent quarks [37]

$$F_{\gamma q}(\mathbf{q}^2)=\frac{1}{1+\mathbf{q}^2/m_\rho^2}. \tag{27}$$

The photon-pion coupling in Fig. 3(d) has the same e.m. form factor in order that the total pion current satisfies the continuity equation with the one-pion exchange potential.

III. RESULTS

In this section, we give our results for the e.m. coupling of the positive parity resonances $P_{33}(1232)$ and $P_{11}(1440)$, and the two negative parity states $S_{11}(1535)$ and $D_{13}(1520)$. The photocouplings of these resonances have already been discussed in Ref. [16]. The new points of this paper are the investigation of the e.m. helicity amplitudes for finite four momentum transfer, and the inclusion of configuration mixing for the positive parity states. Furthermore, we study the scalar helicity amplitudes of the $\Delta(1232)$ and $N^*(1440)$ resonances. No attempt has been made to fit the e.m. helicity amplitudes. After calculating the admixture coefficients in the baryon wave functions and the baryon masses the model is fixed.

As conventional, the e.m. γNN^* coupling is expressed in terms of the transverse (A_λ) and scalar (S_λ) helicity amplitudes originally defined in [3,10]:

$$A_\lambda(\mathbf{q}^2)=-e\sqrt{\frac{2\pi}{\omega}}\langle N^*,M_{J_f}=\lambda|\boldsymbol{\epsilon}_1\cdot\mathbf{J}(\mathbf{q})|N,M_{J_i}=\lambda-1\rangle, \tag{28}$$

$$S_\lambda(\mathbf{q}^2)=e\sqrt{\frac{2\pi}{\omega}}\langle N^*,M_{J_f}=\lambda|\rho(\mathbf{q})|N,M_{J_i}=\lambda\rangle, \tag{29}$$

where ω is the energy transfer and $\boldsymbol{\epsilon}_1=-(\mathbf{e}_x+i\mathbf{e}_y)/\sqrt{2}$ the right circular polarization of the photon. The transverse helicity amplitudes A_λ describe the transition of the nucleon to an excited state (N^*) through the absorption of a spatial photon $\mathbf{A}=\boldsymbol{\epsilon}_1\exp(-i\mathbf{q}\cdot\mathbf{x})$ with positive helicity (spin 1 of photon along z axis). $A_{1/2}$ describes the case when γ and N spin projections are antiparallel and $A_{3/2}$ when they are parallel (see Fig. 1). Thus, the transverse helicity amplitudes are the matrix elements of the spherical $\mathbf{J}_1$ component of the spatial current. The transverse helicity amplitudes can be related to the electric and magnetic (Sachs) form factors for the $\gamma+N\to N^*$ transition by expanding the current operator $\mathbf{J}(\mathbf{q})$ into electromagnetic multipoles. Similarly, the scalar helicity amplitudes S_λ describe the transition induced by the time component of the photon field A_0, i.e., the scalar Coulomb potential Φ with zero spin projection. After a multipole expansion of the charge density $\rho(\mathbf{q})$, they can be related to the Coulomb transition (Sachs) form factors (see the Appendix).

The helicity amplitudes contain all information about the γNN^* vertex. We obtain two independent helicity amplitudes $(S_{1/2},A_{1/2})$ for resonances with $J_f=1/2$, corresponding to two e.m. transition form factors, and three helicity amplitudes $(S_{1/2},A_{1/2},A_{3/2})$ for excitations with total angular momentum $J_f=3/2$, corresponding to three e.m. transition form factors.

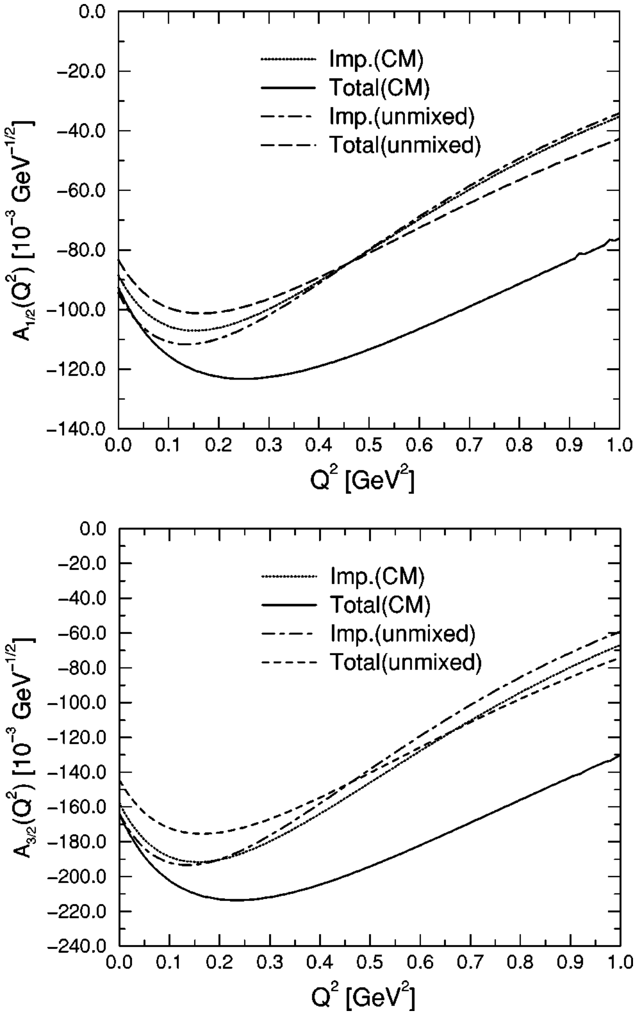

FIG. 4. The transverse $A_{1/2}$ and $A_{3/2}$ helicity amplitudes of the $\gamma N\to P_{33}(1232)$ transition as a function of the four-momentum transfer $Q^2=-q_\mu^2$. The energy transfer of the photon in Eq. (28) is kept fixed to its $Q^2=0$ value in the γN center of mass system, i.e., to $\omega_{\text{c.m.}}=258$ MeV. The dashed-dotted curve [Imp. (unmixed)] is the one-body current evaluated between unmixed wave functions. The dotted curve [Imp. (CM)] is the one-body current calculated with configuration mixing in the wave functions. The dashed curve [Total (unmixed)] includes all spatial currents of Fig. 2 evaluated between unmixed wave functions, and the full curve [Total (CM)] uses the total spatial current calculated with mixed wave functions.

A. The electromagnetic excitation of the $\Delta(1232)$

1. The $N\to\Delta(1232)$ magnetic dipole transition

The transverse helicity amplitudes $A_{1/2}$ and $A_{3/2}$ for $\gamma N\to\Delta$ transition are shown in Fig. 4. We observe that two-body exchange currents do not drastically modify the prediction of the single quark transition model but that the combination of two-body currents and configuration mixing has a sizeable effect at higher momentum transfers.

The transverse helicity amplitudes are completely determined by the magnetic dipole ($M1$) mode as can be seen from the multipole analysis in Table IV. In the single quark transition model, the $M1$ transition is described by the spin-isospin flip of a single quark, and related to the proton magnetic moment by the Beg-Lee-Pais (BLP) relation

$$\mu_{p\to\Delta}=\frac{2\sqrt{2}}{3}\mu_p=-\sqrt{2}\mu_n. \tag{30}$$

In the last step the $SU(6)$ relation $\mu_p/\mu_n=-3/2$ has been used. Equation (30) underestimates the data by about 30%. The problem exists since the early investigations of Dalitz and Sutherland [12], Copley *et al.* [3], Koniuk and Isgur [4]. These authors used h.o. states for the baryon wave functions and the impulse approximation for the e.m. transition operator.

We have studied the effect of two-body exchange currents on the $M1$ excitation of the Δ before. In Refs. [15,16] we

TABLE IV. Transverse (A) and scalar (S) helicity amplitudes of the $\gamma N \rightarrow P_{33}(1232)$ transition at $Q^2=0$ in 10^{-3} GeV$^{-1/2}$ including exchange currents and configuration mixing. Results with configuration mixed wave functions and parameter set II; the numbers in parentheses are calculated with unmixed wave functions and parameter set I. A_i=impulse, A_g=gluon, $A_{\pi q\bar{q}}$=pion pair, $A_{\gamma\pi\pi}$=pion-in-flight, A_c=confinement, and A_σ=sigma meson exchange current contributions. $A_{\rm tot}$ is the sum of all spatial current contributions. The $M1$ and $E2$ parts of $A_{1/2}$ and $A_{3/2}$ are separately given. $(E2)_{\mathbf{J}}$ refers to the spatial currents of Fig. 2; $(E2)_{\rm tot}$ contains the contribution of the two-body charge density $\rho_{[2]}$ using Siegert's theorem. The double spin-flip term contained in $\rho_{[2]}$ of Eq. (22) gives the most important contribution to the electric quadrupole transition. See Ref. [15] for further explanation.

$P_{33}(1232)$	A_i	A_g	$A_{\pi q\bar{q}}$	$A_{\gamma\pi\pi}$	A_c	A_σ	$A_{\rm tot}$	Exp. [11]
$A_{1/2}(M1)$	−90.3	−9.2	13.7	−17.1	19.7	−10.9	−94.1	−149.4
	(−94.4)	(−9.9)	(13.9)	(−16.8)	(34.7)	(−10.9)	(−83.3)	
$A_{1/2}(E2)_{\mathbf{J}}$	1.9	−0.1	0.4	−0.2	−0.5	0.0	1.5	
	(0)	(0)	(0)	(0)	(0)	(0)	(0)	
$A_{1/2}(E2)_{\rm tot}$	1.9	5.3	3.3	−0.2	0.1	0.0	10.4	13.7
	(0)	(6.0)	(2.9)	(0)	(0)	(0)	(8.9)	
$A_{1/2}(\rm tot)$	−88.4	−3.9	17.0	−17.3	19.8	−10.9	−83.7	−135.7±5.5
	(−94.4)	(−3.9)	(16.8)	(−16.8)	(34.7)	(−10.9)	(−74.5)	
$A_{3/2}(M1)$	−156.4	−15.9	23.8	−29.6	34.1	−18.8	−162.9	−258.8
	(−163.5)	(−17.1)	(24.2)	(−29.1)	(60.4)	(−18.0)	(−144.3)	
$A_{3/2}(E2)_{\mathbf{J}}$	−1.1	0.1	−0.3	0.1	0.3	0.0	−0.9	
	(0)	(0)	(0)	(0)	(0)	(0)	(0)	
$A_{3/2}(E2)_{\rm tot}$	−1.1	−3.0	−2.0	0.1	−0.1	0.0	−6.1	−7.9
	(0)	(−3.5)	(−1.7)	(0)	(0)	(0)	(−5.2)	
$A_{3/2}(\rm tot)$	−157.5	−19.0	21.8	−29.5	34.0	−18.8	−169.0	−266.9±9.4
	(−163.5)	(−20.6)	(22.5)	(−29.1)	(60.4)	(−18.0)	(−148.3)	
$S_{1/2}(C2)$	0.7	5.1	2.7	0.0	0.6	0.0	9.1	12.9
	(0.0)	(5.8)	(2.7)	(0.0)	(0.0)	(0.0)	(8.4)	

have used unmixed h.o. wave functions and found no increase in the theoretical $M1$ strength compared to the impulse approximation result of Eq. (30). This is due to a cancellation of various exchange current contributions. A related cancellation has been found for the exchange current contribution to the nucleon magnetic moments [14]. The present calculation shows that an enlargement of the Hilbert space and the use of a more realistic confinement potential does not significantly reduce the discrepancy with experiment. A similar result was obtained by Capstick [9]. There, the relativistically extended one-body current has been evaluated between relativized wave functions including h.o. states up to $N=6$, but the discrepancy between theory and experiment remained at the 30% level. Another relativistic calculation [38] gave values 30–40 % below the experimental amplitude.

Table IV shows the $A_{1/2}$ and $A_{3/2}$ helicity amplitudes with and without (numbers in parentheses) configuration mixing. One notes that the overall effect of configuration mixing is small and the total amplitudes do not differ appreciably from the ones obtained earlier with unmixed wave functions [15,16].

Table V compares our results with other models. Our results qualitatively agree with those found in other models. The ratio between the experimental transition strength and most model predictions is $A_{1/2}^{\rm theory}/A_{1/2}^{\rm exp}\approx 0.7$, i.e., a 30% deviation. Compared to the good agreement of the CQM prediction for the nucleon magnetic moments [14] with experiment, this is a disturbing discrepancy. Configuration mixing in combination with the use of standard two-body current operators does not solve this problem.

Recently, we have studied the effect of two-body retardation currents and three-body currents on the $N \rightarrow \Delta$ transition magnetic moment. In a quark model with gluon exchange as residual interaction, one finds that both effects are too small to explain the empirical value [42]. On the other hand, it has been shown that gluon type three-body currents may increase $\mu_{p\rightarrow\Delta^+}$ to the empirical value [43]. However, the $N\rightarrow\Delta$ transition magnetic moment is closely related to the diagonal Δ^+ magnetic moment μ_{Δ^+}. A large three-body current con-

TABLE V. Transverse helicity amplitudes of the $\gamma N \rightarrow P_{33}(1232)$ transition at $Q^2=0$ in various nucleon models in comparison with the quark model with exchange currents (set II). All entries are in units of 10^{-3} GeV$^{-1/2}$.

$P_{33}(1232)$	[39]	[40]	[41]	[8]	[6]	[9]	[38]	[19]	II	Exp. [11]
$A_{1/2}(Q^2=0)$	−91	−101	−113	−81	−101	−108	−107	−75	−84	−141±5
$A_{3/2}(Q^2=0)$	−157	−186	−195	−170	−176	−186	−189	−131	−169	−258±6

tribution to $\mu_{p\to\Delta^+}$ will lead to a very small μ_{Δ^+}, i.e., a large violation of $SU(6)$ spin-flavor symmetry [44]. A measurement of μ_{Δ^+} would therefore be a quantitative test of the predictions of $SU(6)$ spin-flavor symmetry. A $\gamma p \to \gamma' p' \pi^0$ experiment sensitive to the Δ^+ magnetic moment [45] is currently being carried out at MAMI in Mainz [46].

Finally, the exact value of the M_{1+} pionproduction multipole is uncertain [47] as is the method of extraction of the γNN^* vertex from the physical amplitude shown in Fig. 1; it cannot be excluded that the intrinsic $N\to\Delta$ transition magnetic moment extracted from the data is actually close to $\mu_{p\to\Delta^+}=3.0\,\mu_N$ and the violation of $SU(6)$ spin-flavor symmetry is compatible with that observed in other baryon magnetic moments.

In summary, there is a close connection between the $N\to\Delta$ magnetic dipole transition and the nucleon magnetic form factors, as given by the Beg-Lee-Pais relation in Eq. (30). The inclusion of exchange currents does not break this relation [21]. This does not only hold for unmixed wave functions, where the relation is a consequence of the spin-flavor $SU(6)$ symmetry, but also for configuration mixed states.

2. The N→Δ(1232) quadrupole transition

Considerable theoretical and experimental effort has been devoted to the extraction of the $N\to\Delta$ quadrupole transition strength from the pion production data [48]. The scalar charge quadrupole ($C2$) and transverse electric quadrupole ($E2$) transitions and the related $C2/M1$ and $E2/M1$ ratios give information about the intrinsic deformation of the nucleon. In the single-quark transition model, the nonvanishing $C2$ amplitude has been attributed to the D-state admixtures in the N and Δ wave functions (D waves in the nucleon) [49]. However, recent work in the quark model with two-body exchange currents has shown that the $E2$ and $C2$ transition amplitudes to the Δ are not governed by the small D-state components in the nucleon and Δ wave function. Instead, the quark-antiquark pair currents of Figs. 3(b) and 3(c) give the dominant contribution to the $N\to\Delta$ quadrupole transition in the CQM [15].

Figure 5 shows the influence of exchange currents and configuration mixing on the scalar helicity amplitude at finite moment transfers. For unmixed wave functions the $C2$ amplitude vanishes in impulse approximation, and is completely given by the exchange current diagrams of Figs. 3(b) and 3(c) (dashed-dotted curve), in particular by the spin tensor (double spin-flip term) in the two-body charge operator [see Eq. (33)]. Evidently, this double spin flip term dominates not only at $Q^2=0$ but also for finite momentum transfers. For mixed wave functions there is a small one-body contribution shown by the dotted curve, which enhances the double spin flip term by some 30% at intermediate momentum transfers.

There exist various definitions of the $C2/M1$ ratio. Experimentalists usually define it in terms of the measured pion production multipoles S_{1+} and M_{1+} while theorists prefer a definition in terms of the helicity amplitudes $S_{1/2}$ and $A_{1/2}$, which describe the γNN^* vertex directly [56]. If the photon energy transfer is equal to

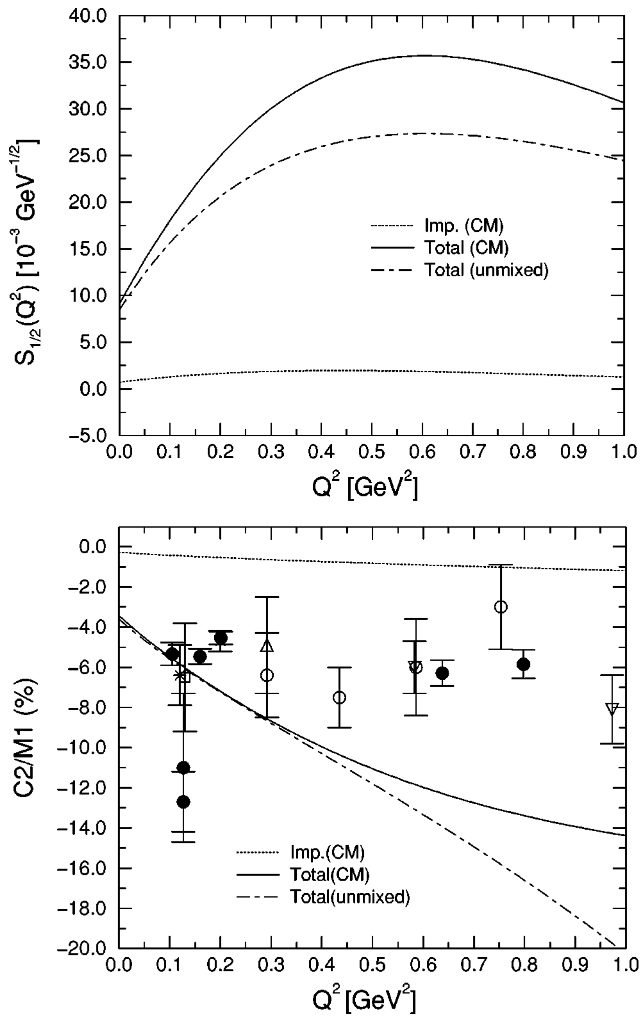

FIG. 5. Scalar $S_{1/2}$ helicity amplitude of the $\gamma N\to P_{33}(1232)$ transition and the $C2/M1$ ratio as a function of the photon four-momentum transfer. The energy transfer of the photon in Eq. (28) is kept fixed to its $Q^2=0$ value in the γN center of mass system, i.e., to $\omega_{\mathrm{c.m.}}=258$ MeV. The dotted curve [Imp. (CM)] is calculated with the one-body current from Fig. 3(a) and mixed wave functions. The dashed-dotted curve [Total (unmixed)] uses the total current evaluated between unmixed wave functions. The full curve [Total (CM)] is our result including the two-body exchange currents of Figs. 2(b)–2(e) evaluated between mixed wave functions. The results for the proton and neutron excitation are the same. The experimental data are from Refs. [50] (▽), [51] (△), [52] (○), [53] (□), [54] (*), and [55] (●).

$$\omega_{\mathrm{c.m.}}=\frac{M_\Delta^2-M_N^2-Q^2}{2M_\Delta} \tag{31}$$

corresponding to Δ resonance excitation in the hadronic rest frame, the pion production multipoles can be expressed via the $\gamma N\to\Delta(1232)$ helicity amplitudes and one can write the $C2/M1$ ratio as follows [24]:

$$\frac{C2}{M1}(\mathbf{q}^2)=\frac{1}{2\sqrt{2}}\,\frac{S_{1/2}(C2)(\mathbf{q}^2)}{A_{1/2}(M1)(\mathbf{q}^2)}=\frac{|\mathbf{q}|M_N}{6}\,\frac{F_{C2}(\mathbf{q}^2)}{F_{M1}(\mathbf{q}^2)}. \tag{32}$$

The connection between the helicity amplitudes $S_{1/2}$ and $A_{1/2}$ and the $N \rightarrow \Delta$ charge quadrupole and magnetic dipole form factors F_{C2} and F_{M1} calculated in Refs. [15,18] is given in the Appendix. In the limit $\mathbf{q} \rightarrow 0$ we find $C2/M1 = 0$, and at the real photon point we obtain $C2/M1 = -0.036(-0.035)$ with (without) configuration mixing.

The main contribution to the $C2/M1$ ratio comes from the tensor term in the exchange charge operator, which, e.g., for gluon exchange [see Eq. (22)] can be rewritten as [57]

$$\rho_{[2]}(C2) = B \sum_{i<j} e_i (3\sigma_{iz}\sigma_{jz} - \boldsymbol{\sigma}_i \cdot \boldsymbol{\sigma}_j), \tag{33}$$

where B stands for the color and radial part. The matrix elements of the above operator exceed the single-quark transition amplitude by a large factor. The reason for the dominance of the $\rho_{[2]}$ term is easy to understand. In impulse approximation (dotted curve), the scalar transition amplitude $S_{1/2}$ receives the main contribution from the $S \rightarrow D$ (and $D \rightarrow S$) transitions. Because the D-state components in the nucleon and Δ wave functions are very small compared to the dominant S waves (see Table II), the amplitude $S_{1/2}$ calculated in impulse approximation is close to zero (see Fig. 5) and much too small compared with experiment. On the other hand, the spin tensor term in Eq. (33) induces a double spin-flip transition between the S state in the $N(939)$ and the S state in the $\Delta(1232)$ [15]. No D states are required to make this double spin flip quadrupole transition from the N to the Δ.

At small momentum transfers our theory is in good agreement with the data. At higher momentum transfers most data from the beginning of the 1970s are slightly above our CQM calculation. Using the quark model relation between the $N \rightarrow \Delta$ and the neutron charge and magnetic form factors [21] one can express the $C2/M1$ ratio in electro-pionproduction in terms of the elastic neutron form factors. The $C2/M1$ ratio predicted from the neutron elastic form factor *data* is in better agreement with the electro-pionproduction data than the explicit quark model calculation [58]. We conclude that exchange currents dominate the $C2/M1$ ratio. Their inclusion significantly reduces the discrepancy between the impulse approximation and experiment.

The $E2/M1$ ratio is defined as in Ref. [15]

$$\frac{E2}{M1}(\mathbf{q}^2) = \frac{1}{3}\frac{A_{1/2}(E2)(\mathbf{q}^2)}{A_{1/2}(M1)(\mathbf{q}^2)} = \frac{\omega_{\mathrm{c.m.}} M_N}{6}\frac{F_{C2}(\mathbf{q}^2)}{F_{M1}(\mathbf{q}^2)} \tag{34}$$

and plotted in Fig. 6. In the last equation we have made use of Siegert's theorem which relates the $C2$ and the $E2$ multipoles in the low-momentum transfer region [15]. In contrast to the $C2/M1$ ratio we observe a sign change at $Q^2 = 0.64\ \mathrm{GeV}^2$ as in Ref. [60]. In our theory, this is due to the kinematical factor in Eq. (31). While the energy transfer $\omega_{\mathrm{c.m.}}$ in the normalization factor $\sqrt{2\pi/\omega_{\mathrm{c.m.}}}$ of the $A_{1/2}$ and $A_{3/2}$ helicity amplitudes in Eq. (28) is kept fixed in order to keep the individual helicity amplitudes finite [8], the kinematical factor $\omega_{\mathrm{c.m.}}$ entering the definition of $E2/M1$ ratio in Eq. (34) must be considered as a function of four-momentum transfer Q^2. In [18] we kept $\omega_{\mathrm{c.m.}}$ appearing in the definition of $E2/M1$ fixed to 258 MeV, and no sign change occurred.

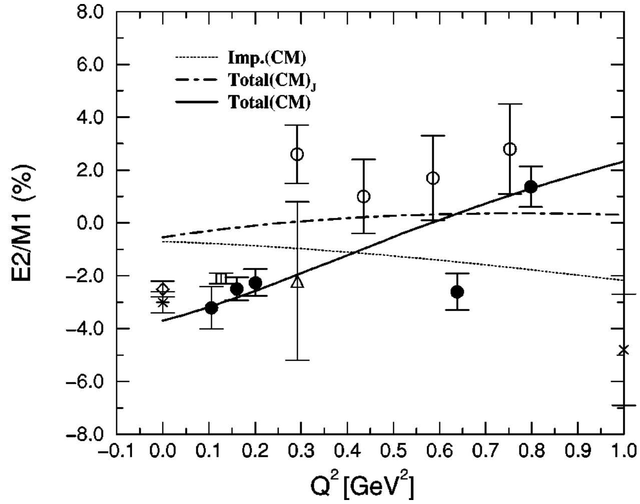

FIG. 6. $E2/M1$ ratio of the $\gamma N \rightarrow P_{33}(1232)$ transition amplitudes as a function of the four-momentum transfer Q^2. The dotted curve [Imp. (CM)] is calculated in impulse approximation with configuration mixing (CM) in the baryon wave functions. The dashed-dotted curve [Total (CM)]$_J$ takes the spatial exchange currents of Fig. 2 into account. The full curve [Total (CM)] contains the contribution of the two-body charge density $\rho_{[2]}$ using Siegert's theorem (see Ref. [15] for further explanation). The experimental values are from Refs. [22] (◇), [23] (*), [51] (△), [52] (○), [53] (□), [55] (●), and [59] (×).

A sign change from negative to positive $E2/M1$ at a certain Q^2 is expected from perturbative QCD. According to quark helicity conservation the $E2/M1$ ratio will asymptotically approach unity [61]

$$\lim_{Q^2 \rightarrow \infty} \frac{E2}{M1} = 1.$$

In the low momentum transfer limit $\mathbf{q} \rightarrow 0$, we obtain without configuration mixing the simple result [15]

$$\frac{E2}{M1}(\mathbf{q} \rightarrow 0) = \frac{\omega_{\mathrm{c.m.}} M_N}{6}\frac{Q_{p\rightarrow\Delta}}{\mu_{p\rightarrow\Delta}} = -\frac{(M_\Delta - M_N)M_N}{12}\frac{r_n^2}{\mu_n}, \tag{35}$$

using the relations in Eqs. (1) and (2). With (without) configuration mixing we obtain $E2/M1 = -0.040(-0.035)$.

In summary, a comparison of the $C2/M1$ and $E2/M1$ ratios with and without exchange currents shows that the quark-antiquark pair currents in Fig. 3 are necessary to correctly describe these ratios in the CQM. This suggests that the quadrupole transition proceeds mainly via an excitation of the peripheral $q\bar{q}$ cloud degrees of freedom. Recently, this picture has been used to estimate the intrinsic quadrupole moment of the N and Δ in the CQM [57]. The intrinsic quadrupole moment of the $N(\Delta)$ is found to be positive (negative) corresponding to a prolate (oblate) intrinsic deformation.

TABLE VI. Transverse helicity amplitudes of the $\gamma N \to P_{11}(1440)$ transition at $Q^2=0$ calculated in different nucleon models. Details of the present calculation (II) are given in Table VII.

$P_{11}(1440)$	[39]	[40]	[41]	[9]	[6]	[64]	[65]	II	Exp. [11]
$A^p_{1/2}(Q^2=0)$	+67	−30	+10	+4	−5	−77	−66	−90	−65±4
$A^n_{1/2}(Q^2=0)$	−45	+19	−11	−6	+4	+35	+44	+56	40±10

B. The electromagnetic excitation of the $N^*(1440)$

The $P_{11}(1440)$ (Roper) resonance is one of the most interesting excitation modes of the nucleon. It is the lowest lying nucleon resonance with the same spin, orbital angular momentum, parity, and isospin as the nucleon ground state. In the h.o. quark model it is described as an $N=2$ radial excitation, corresponding to a spherically symmetric expansion and contraction of the three-quark core radius (breathing mode). It should therefore have a higher energy than the $S_{11}(1535)$ and $D_{13}(1520)$ nucleon resonances with $N=1$ and negative parity. This is not observed experimentally. A calculation of the Roper resonance excitation in a coupled channel meson-nucleon model provides evidence for an exceptionally strong coupling of the resonant three-quark state with nonresonant meson-baryon (σN, $\pi\Delta$) scattering channels [62]. This strong channel coupling may be responsible for the low Roper mass and its peculiar e.m. properties. Another possibility is that the Roper is strongly deformed. In a deformed h.o. quark model the positive parity $N=2$ excitation has a lower energy than the $N=1$ negative parity state [63].

Also with respect to its electromagnetic coupling, the Roper resonance is rather different compared to other nucleon resonances. At present, no quark model is able to describe the experimental e.m. coupling of the Roper satisfactorily. If only single quark currents are considered, the photocouplings of the proton and neutron are underestimated by a factor of 2 or more (see Table VI and Table VII). In contrast, at finite momentum transfers the absolute values of the calculated transverse and scalar helicity amplitudes overestimate the data by a large factor in most quark models.

Electroquenching refers to the fact that the $A_{1/2}$ amplitude of the Roper decreases rapidly from its large and negative value at the real photon point to very small values at finite momentum transfers. The helicity amplitudes of most other resonances approach zero only gradually with increasing four-momentum transfer. This peculiar behavior of the Roper resonance cannot be reproduced in most models [8,9,65]. For example, Aiello *et al.* [65] get a good agreement of the e.m. Roper coupling strength at the real photon point. They use a model where three-body forces are included through the use of hyperspherical harmonic wave functions. However, also in their calculations the problem with the electroquenching for finite momentum transfer remains unsolved [66]. A relativized quark model based on the light-front formalism [38] could describe the electroquenching of the helicity amplitudes. However, the problem with simultaneously predicting the empirical value at the real photon point remains. The model of Li *et al.* [13], in which the Roper is characterized by the excitation of explicit gluon degrees of freedom, in addition to the three valence quark configuration describes the e.m. $N \to N^*(1440)$ transition satisfactorily. This approach should be further tested by calculating other e.m. properties of the nucleon, e.g., charge radii.

1. The magnetic dipole excitation of the N*(1440)

In contrast to the magnetic form factors of the $N(939)$ and the magnetic dipole excitation of the $\Delta(1232)$, the two-body currents add constructively in the $M1$ excitation of the $N^*(1440)$. This result was already obtained in Ref. [16] using unmixed wave functions. It is confirmed in the present calculation including configuration mixing.

At the real photon point (Table VII), exchange currents improve the agreement with the data for the neutron excitation. For the proton, the total result including exchange currents overestimates the experimental coupling of the Roper

TABLE VII. Transverse (A) and scalar (S) helicity amplitudes of the $\gamma N \to P_{11}(1440)$ excitation at $Q^2=0$ in units of 10^{-3} GeV$^{-1/2}$. The calculations are based on (i) configuration mixed wave functions, parameter set II, and a theoretical mass of 1533 MeV; (ii) unmixed wave functions, parameter set I, and a theoretical mass of 1440 MeV (numbers in parentheses). For further explanation see Table IV.

$P_{11}(1440)$	A_i	A_g	$A_{\pi q\bar{q}}$	$A_{\gamma\pi\pi}$	A_c	A_σ	A_{tot}	Exp. [11]
$A^p_{1/2}(M1)$	−25.7	−8.4	+3.4	−6.3	−43.9	−8.9	−89.8	−65±4
	(−29.7)	(−15.8)	(+5.7)	(−12.0)	(−20.4)	(−14.9)	(−87.3)	
$A^n_{1/2}(M1)$	+15.1	+2.6	−3.4	+6.3	+30.0	+5.7	+56.3	+40±10
	(+19.8)	(+5.2)	(−5.7)	(+12.0)	(+13.6)	(+10.0)	(+55.0)	
	S_i	S_g	$S_{\pi q\bar{q}}$	$S_{\gamma\pi\pi}$	S_c	S_σ	S_{tot}	
$S^p_{1/2}(C0)$	−21.8	+5.2	−1.4	0.0	+24.4	+4.7	+11.1	
	(−31.8)	(+7.4)	(−2.6)	(0.0)	(+9.5)	(+6.9)	(−10.5)	
$S^n_{1/2}(C0)$	+7.9	−2.9	−0.8	0.0	+1.8	−0.5	+5.5	
	(+0.0)	(−4.9)	(−1.8)	(0.0)	(0.0)	(0.0)	(−6.7)	

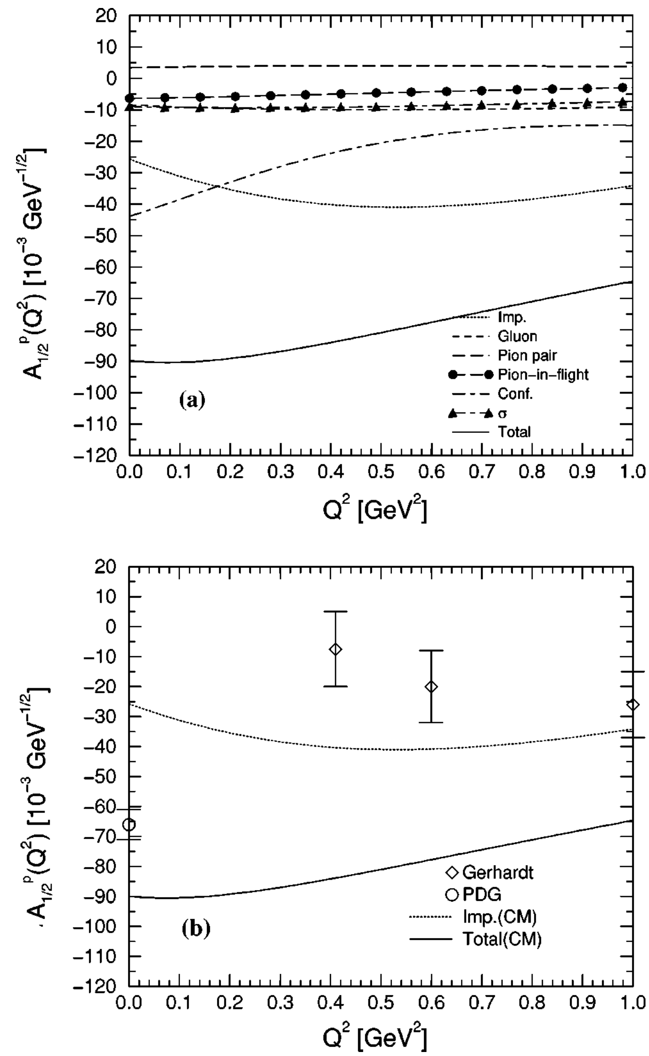

FIG. 7. (a) Transverse $A_{1/2}^{p}$ helicity amplitude of the $\gamma p \rightarrow P_{11}(1440)$ transition as a function of the four-momentum transfer Q^2. The one-body current (dotted curve), the contributions of the different two-body currents, and the sum of one- and two-body currents (full curve) are given separately. (b) The curve labeled Imp. (CM) is the result in impulse approximation including configuration mixing. The curve [Total (CM)] denotes the total $A_{1/2}^{p}$ amplitude with two-body exchange current operators evaluated between mixed wave functions. The experimental results are from Ref. [67] (Gerhardt) and Ref. [11] (PDG).

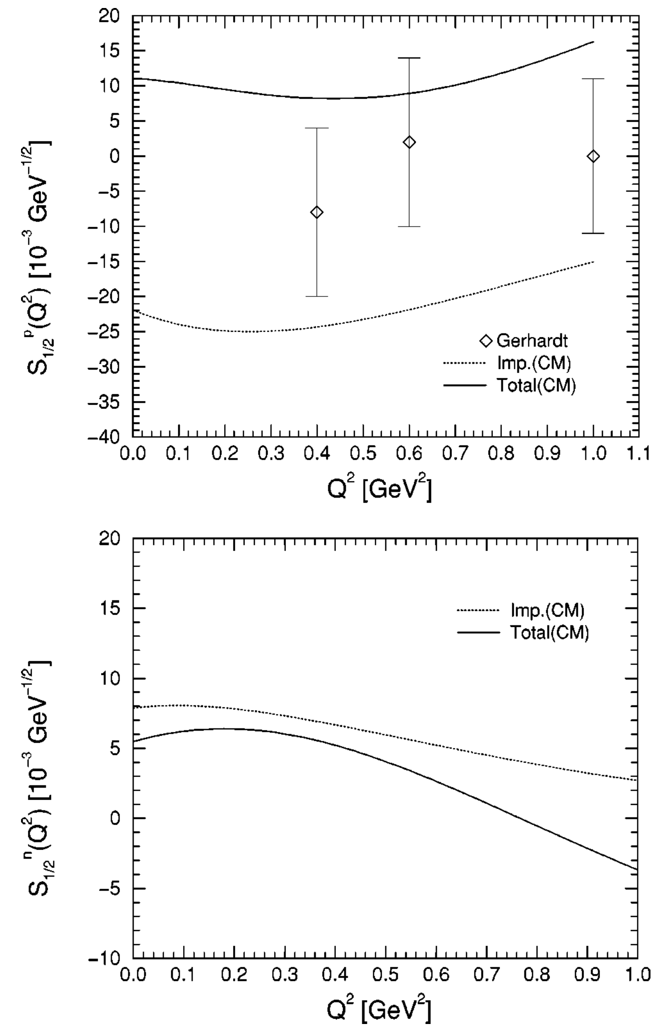

FIG. 8. Scalar $S_{1/2}$ helicity amplitude of the $\gamma N \rightarrow P_{11}(1440)$ transition as a function of the photon four-momentum transfer Q^2. The notation is the same as in Fig. 7(b).

by some 30%. Nevertheless, it is closer to the data than the impulse approximation. We emphasize that the sum of all two-body exchange currents is about twice as large as the contribution from the one-body current. Note that the experimental result for $A_{1/2}^{p}/A_{1/2}^{n} \approx -3/2$, corresponding to the ratio of proton and neutron magnetic moments is also obtained after inclusion of two-body exchange currents. Thus, our theory preserves the success of the single quark transition model, while improving the agreement between theory and experiment for the individual proton and neutron amplitudes. A glance at Table VI shows that this ratio is not always preserved.

The rapid decrease of the $A_{1/2}$ amplitude at finite momentum transfers seen in the data is not described in the present model (Fig. 7). The inclusion of two-body currents does not solve this problem. The experimentally required suppression of the transverse helicity amplitude could only be obtained with an unrealistic large value of the quark core radius b, which however, would be in conflict with the value of b required by most other observables.

2. The Coulomb monopole excitation of the N(1440)*

For the scalar e.m. excitation of the Roper, corresponding to a charge monopole ($C0$) transition, our result is compatible with the experimental data (see Fig. 8). The shape of the impulse approximation curve and the one including exchange currents is qualitatively the same. However, due to the two-body currents, the strength of the coupling is reduced and the agreement with the experimental data is somewhat improved. For the neutron, the effect of the exchange currents is nearly vanishing for small momentum transfers, whereas for momenta from around 0.5 up to 1 GeV^2 two-body currents make an important contribution. In contrast to the impulse approximation, we obtain a sign change at about 0.8 GeV^2.

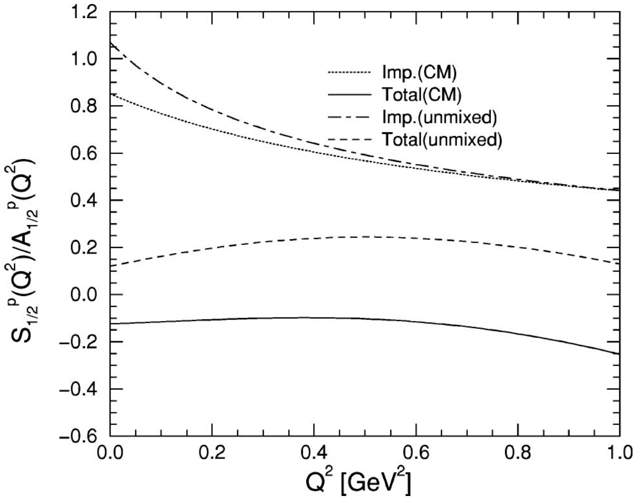

FIG. 9. Ratio of the scalar and transverse coupling of $\gamma p \to P_{11}(1440)$ transition as a function of the four-momentum transfer Q^2. The curves denoted by Total (CM) and Imp. (CM) are the results for the total current and the one-body current evaluated between configuration mixed wave functions. The curves labeled Total (unmixed) and Imp. (unmixed) show the corresponding results with unmixed wave functions.

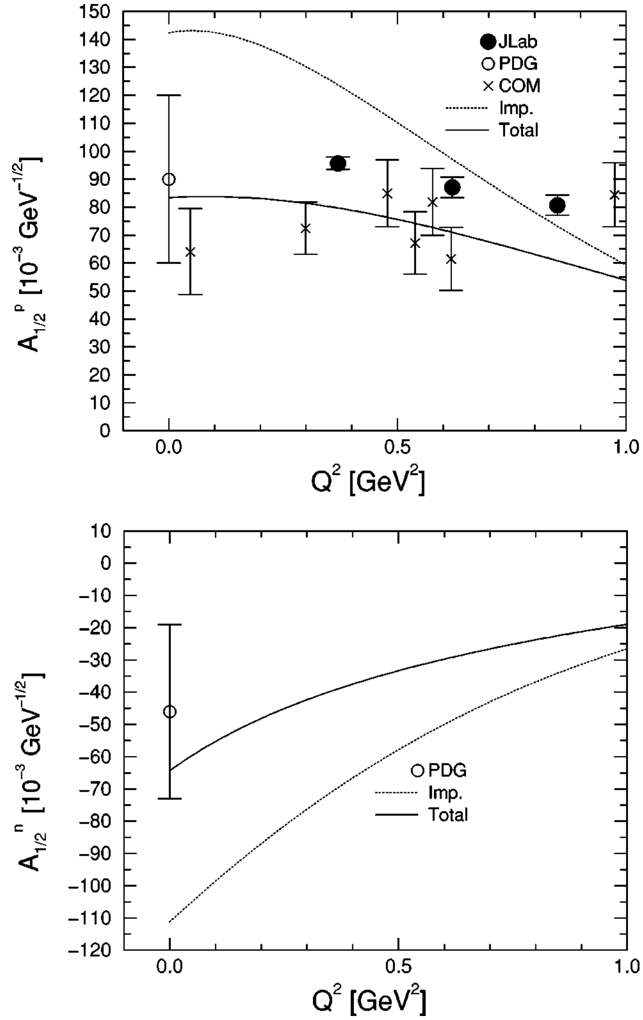

FIG. 10. Transverse $A_{1/2}$ helicity amplitude of the $\gamma N \to S_{11}(1535)$ transition as a function of the photon four-momentum transfer Q^2. The energy transfer of the photon in Eq. (28) is kept fixed to its $Q^2=0$ value in the γN center of mass system. Here, $\omega_{\mathrm{c.m.}}=318$ MeV corresponding to a resonance mass of 1310 MeV obtained with unmixed wave functions. The full curve (Total) is the result for the total current including two-body exchange currents. The dotted curve (Imp.) is the result in impulse approximation. The experimental data are from Ref. [11] (PDG) and from the data compilation of Burkert (COM) as quoted in Ref. [69]. The full circles are recent data taken at Jefferson Lab [71].

A quantity which is supposedly quite insensitive to the size of the Hilbert space of spatial wave functions is the ratio of the scalar and transverse helicity amplitudes, $S_{1/2}/A_{1/2}$ [13], or alternatively the $C0/M1$ ratio. If this assumption is justified, this ratio should be more sensitive to the degrees of freedom included in the e.m. transition operator than to the size of the Hilbert space in which the baryon wave function is expanded. That this is indeed the case can be seen by comparing the curves labeled "unmixed" and "CM" in Fig. 9. The total result including exchange currents is very different from the one-body result. Whereas the impulse approximation (dotted curve) decreases by a factor of two in the range $Q^2=0-1$ GeV^2, the total ratio with exchange currents (full curve) is approximately constant over the entire momentum transfer range considered. Figure 9 shows that the $S_{1/2}/A_{1/2}$ ratio is more sensitive to the dynamical degrees of freedom included in the e.m. current operator than to the size of the h.o. basis. This ratio can therefore be used to isolate the effect of exchange currents in the nucleon. We obtained a similar conclusion for the $E2/M1$ and $C2/M1$ ratios of the e.m. $\Delta(1232)$ excitation. Also these observables provide clear evidence for the importance of two-body currents.

Finally, we remark that our prediction for the $S_{1/2}^{p}/A_{1/2}^{p}$ ratio is completely different from the light-front impulse approximation results [38]. These authors predict a dominance of $S_{1/2}$ in the range $0.2<Q^2<0.6$ GeV^2 and a sign change at $Q^2\approx 0.25$ GeV^2 caused by the transversal $A_{1/2}^{p}$ amplitude.

TABLE VIII. Transverse helicity amplitudes of the $\gamma N \to S_{11}(1535)$ transition in units of 10^{-3} GeV$^{-1/2}$ at the real photon point ($Q^2=0$) without configuration mixing. In contrast to Ref. [16], the calculation is now based on the theoretical mass of 1310 MeV. For further explanation, see Table IV.

$S_{11}(1535)$	A_i	A_g	$A_{\pi q\bar{q}}$	$A_{\gamma\pi\pi}$	A_c	A_σ	A_{tot}	Exp. [11]
$A_{1/2}^{p}(E1)$	$+142.4$	-34.0	-19.3	$+17.4$	-25.7	$+2.7$	$+83.5$	$+90\pm30$
$A_{1/2}^{n}(E1)$	-111.2	$+37.4$	$+19.3$	-17.4	$+8.6$	-1.0	-64.3	-46 ± 27

TABLE IX. Transverse helicity amplitudes of the $\gamma N \to D_{13}(1520)$ coupling in units of $10^{-3}\ \text{GeV}^{-1/2}$ at the real photon point ($Q^2=0$) without configuration mixing. In contrast to Ref. [16] the theoretical mass of 1310 MeV is used. For the notation, see Table IV. The $E1$ and $M2$ multipoles are given separately.

$D_{13}(1520)$	A_i	A_g	$A_{\pi q\bar{q}}$	$A_{\gamma\pi\pi}$	A_c	A_σ	A_{tot}	Exp. [11]
$A^p_{1/2}(E1)$	+51.0	+12.0	−13.6	+12.3	+9.1	−1.0	+69.9	
$A^p_{1/2}(M2)$	−49.6	−7.4	0.0	0.0	+27.3	−2.9	−32.6	
$A^p_{1/2}(E1+M2)$	1.4	4.6	−13.6	+12.3	+36.4	−3.9	+37.3	−24±9
$A^n_{1/2}(E1)$	−62.1	−13.2	+13.6	−12.3	−3.0	+0.3	−76.7	
$A^n_{1/2}(M2)$	+16.5	+3.9	0.0	0.0	−9.1	+1.0	+12.3	
$A^n_{1/2}(E1+M2)$	−45.5	−9.4	+13.6	−12.3	−12.1	+1.3	−64.4	−59±9
$A^p_{3/2}(E1)$	+88.4	+20.8	−23.6	+21.3	+15.8	−1.7	+121.1	
$A^p_{3/2}(M2)$	+28.6	+4.3	0.0	0.0	−15.8	+1.7	+18.8	
$A^p_{3/2}(E1+M2)$	+117.1	+25.1	−23.6	+21.3	0.0	0.0	+139.9	+166±5
$A^n_{3/2}(E1)$	−107.5	−22.9	+23.6	−21.6	−5.3	+0.6	−132.9	
$A^n_{3/2}(M2)$	−9.5	−2.2	0.0	0.0	+5.3	−0.6	−7.1	
$A^n_{3/2}(E1+M2)$	−117.1	−25.1	+23.6	−21.3	0.0	0.0	−139.9	−139±11

C. Electric dipole excitation of the $S_{11}(1535)$ resonance

We turn now to nucleon excitations with negative parity, namely the $S_{11}(1535)$ with total angular momentum $J=1/2$. In the single quark transition model, this resonance corresponds to an $N=1$ orbital $S\to P$ wave excitation of a single quark. After coupling the orbital angular momentum $L=1$ with the quark spin $S=1/2$, one obtains a state with total angular momentum $J=1/2$, which is identified with the $S_{11}(1535)$, and a $J=3/2$ state, the $D_{13}(1520)$. The experimental fact that these states are (almost) energetically degenerate requires that the total spin-orbit force between constituent quarks be very small in this channel. The $S_{11}(1535)$ resonance is mainly observed in the $\gamma+p\to N^*(1535)\to p+\eta$ reaction [68].

Diagonalization of the Hamiltonian shows that the mixing with higher oscillator states is larger for positive than for negative parity resonances. This can be seen from the admixture coefficients calculated by Giannini [5]. Therefore, the results are given only for the unmixed wave functions obtained with parameter set I. In contrast to Ref. [16] where the experimental mass of 1520 MeV has been employed, the theoretical mass of 1310 MeV for unmixed wave functions is used here.

Table VIII lists the transverse helicity amplitude $A_{1/2}$ for the excitation of the $S_{11}(1535)$ resonance. As already pointed out [16] the long-standing problem that the photocoupling to the $S_{11}(1535)$ is overestimated in impulse approximation disappears after including two-body exchange currents. Exchange currents strongly reduce the photocoupling, and the total result is in better agreement with the data.

At finite Q^2, the experimental helicity amplitude is well described for low momentum transfers, but falls off too fast for $Q^2>1\ \text{GeV}^2$ (Fig. 10). In this kinematical region the difference between impulse approximation and the total current is small, and exchange currents do not reduce the discrepancy between theory and experiment. However, one should not forget that momentum transfers of 1 GeV are probably beyond the region of validity of the nonrelativistic potential model.

For the neutron, there is only one datum at the real photon point. Exchange currents reduce the result obtained in the single quark transition model by approximately a factor of 2 (Table VIII and Fig. 10) in agreement with the data. This reduction only occurs for momentum transfers below $1\ \text{GeV}^2$. For higher momentum transfers the results with and without exchange currents are nearly the same.

D. Electromagnetic excitation of the $D_{13}(1520)$ resonance

In the CQM, the D_{13} resonance corresponds to a P wave excitation of a single quark, where the orbital angular momentum $L=1$ and the spin $S=1/2$ of the three-quark state are coupled to total angular momentum $J=3/2$. Table IX lists the $A_{1/2}$ and $A_{3/2}$ helicity amplitudes at the real photon point. Note that the experimental $A^p_{3/2}$ amplitude is very large whereas $A^p_{1/2}$ is comparatively small. In the single quark transition model, the $A^p_{3/2}$ amplitude is smaller than the experimental result. In order to solve this problem, the use of a smaller quark core radius of about $b=0.48$ fm has been suggested [3]. As a result of this choice a cancellation between the spin and convection part of the one-body current in Eq. (16) appeared and the $A_{1/2}$ amplitude could be made very small while the $A_{3/2}$ amplitude could be increased. The fact that the required value for the size parameter b was not completely unreasonable was considered as an early success of the quark model [70]. On the other hand, the same model requires $b\approx 1$ fm in order to describe the neutron charge radius [5,14]. We adhere to the value of $b=0.613$ fm, which was obtained from the nucleon stability condition as described in Sec. II B. This value for b is also consistent with the empirical neutron charge radius if exchange currents are included [14].

We find that the inclusion of exchange currents allows us to improve the agreement between theory and experiment for the $\gamma N \rightarrow D_{13}(1520)$ transition and the nucleon charge radii using a single size parameter $b = 0.613$ fm for both observables. For the $A^p_{3/2}$ amplitude, a discrepancy of about 15% between theory and experiment remains, whereas the agreement is perfect for the neutron. We obtain both for the one-body current and for the total current the relation $A^p_{3/2} = -A^n_{3/2}$. The deviation from this relation inherent in the data indicates the importance of configuration mixing for the negative parity states.

While the inclusion of two-body currents improves the agreement with experiment for both $A^p_{3/2}$ and $A^n_{3/2}$ amplitudes, the small $A^p_{1/2}$ amplitude differs very much from the experimental value. This is partly connected with the fact that the calculated resonance mass of 1310 MeV is 200 MeV lower than the experimental value. For the neutron $A^n_{1/2}$ amplitude the situation looks much better. Due to the exchange currents we obtain a result which is within the experimental error bars.

Additional evidence for the importance of exchange currents in the negative parity states comes from comparing the $A^n_{1/2}(S_{11})$ and $A^n_{1/2}(D_{13})$ amplitudes. The single quark transition model (see columns A_i in Table VIII and Table IX) predicts that $A^n_{1/2}(S_{11})$ dominates over $A^n_{1/2}(D_{13})$ in disagreement with experiment. After including two-body exchange currents, the $A^n_{1/2}(S_{11})$ amplitude is reduced and the $A^n_{1/2}(D_{13})$ is enhanced in agreement with the data.

Figures 11 and 12 show the transverse helicity amplitudes for the $\gamma N \rightarrow D_{13}(1520)$ excitation. At finite Q^2 no experimental data are available for the neutron. The calculated $A^p_{3/2}$ amplitude falls off too rapidly above 0.5 GeV^2. Around $Q^2 = 0$, the $A^p_{3/2}$ helicity amplitude for $\gamma p \rightarrow D_{13}(1520)$ is much larger than the corresponding $A^p_{1/2}$ amplitude (see Table IX). In contrast to this, $A^p_{1/2}$ dominates over $A^p_{3/2}$ for higher momentum transfers according to quark helicity conservation. This behavior is also reflected in the dominance of the $E1$ $(M2)$ amplitude for small (large) momentum transfers.

The relative size of the $A_{1/2}$ and the $A_{3/2}$ amplitudes is often expressed via the helicity asymmetry [1]:

$$A_{1/2,3/2} = \frac{A^2_{1/2} - A^2_{3/2}}{A^2_{1/2} + A^2_{3/2}}. \tag{36}$$

From the multipole expansion of the helicity amplitudes (see the Appendix)

$$A_{1/2} = A_{1/2}(E1) + A_{1/2}(M2),$$

$$A_{3/2} = \sqrt{3} A_{1/2}(E1) - \frac{1}{\sqrt{3}} A_{1/2}(M2), \tag{37}$$

we see that the asymmetry gives $A_{1/2,3/2} = \pm 1/2$ when one multipole vanishes. In the present model, $A_{1/2,3/2} = -1/2$ is obtained at $\mathbf{q}^2 = 0$, where the $M2$ amplitude vanishes. Furthermore, as a consequence of hadronic helicity conservation one finds $A_{3/2}(Q^2 \rightarrow \infty) = 0$, $A_{1/2,3/2} = 1$, and $A_{1/2}(M2) = 3A_{1/2}(E1)$. In the limit $Q^2 \rightarrow 0$, $A_{3/2}$ dominates, $A_{1/2,3/2} = -1$, and $A_{1/2}(M2) = -A_{1/2}(E1)$. As can be seen from Fig. 11 and Fig. 13 this behavior is reproduced for the proton and neutron. Both for the proton and neutron (where again only the value at $Q^2 = 0$ is given for comparison), the exchange currents improve the agreement with the experimental data.

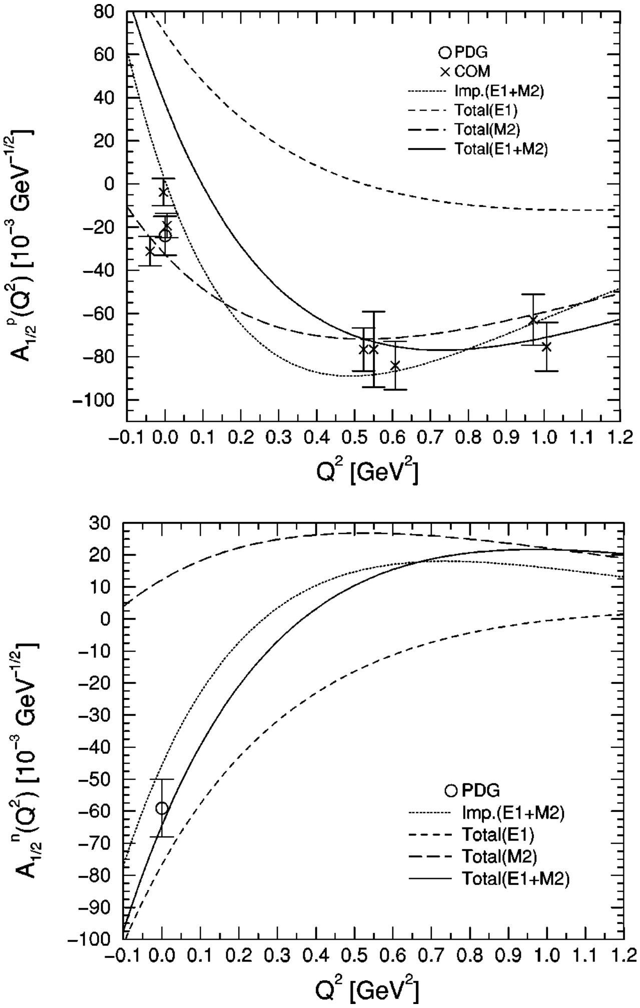

FIG. 11. Transverse $A_{1/2}$ helicity amplitude of the $\gamma N \rightarrow D_{13}(1520)$ transition as a function of the photon four-momentum transfer Q^2. The energy transfer of the photon in Eq. (28) is kept fixed to its $Q^2 = 0$ value in the γN center of mass system. Here, $\omega_{\mathrm{c.m.}} = 318$ MeV corresponding to a resonance mass of 1310 MeV obtained with unmixed wave functions. The dotted curve is the impulse approximation (Imp.). The full curve includes the two-body exchange currents. The short-dashed curve shows the total electric dipole [Total (E1)] and the long-dashed curve the total magnetic quadrupole [Total (M2)] contributions. The experimental data are from Ref. [11] and from the data compilation of Burkert (COM) as quoted in Ref. [69].

IV. SUMMARY

We have extended our previous calculation of the transverse helicity amplitudes for the photoproduction of the $P_{33}(1232)$, $P_{11}(1440)$, $S_{11}(1535)$, and $D_{13}(1520)$ nucleon resonances to electroproduction. A constituent quark model with residual gluon, pion, and sigma-exchange interactions including the corresponding two-body exchange currents has

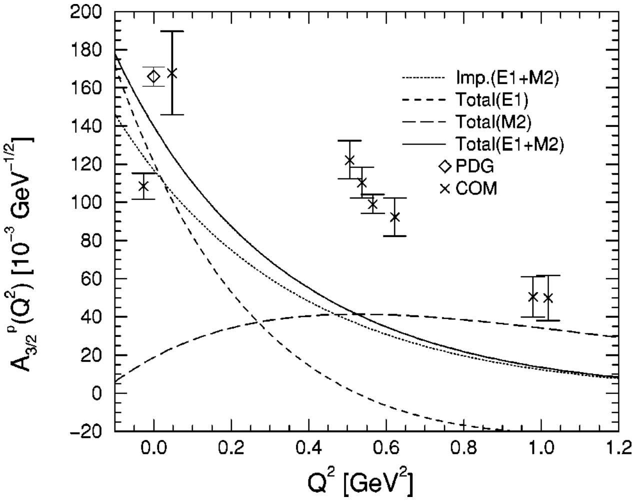

FIG. 12. Transverse $A_{3/2}$ helicity amplitude of the $\gamma p \to D_{13}(1520)$ transition as a function of the photon four-momentum transfer Q^2. The experimental data are from Ref. [11] (PDG) and from the data compilation of Burkert (COM) as quoted in Ref. [69]. For further explanation, see Fig. 11.

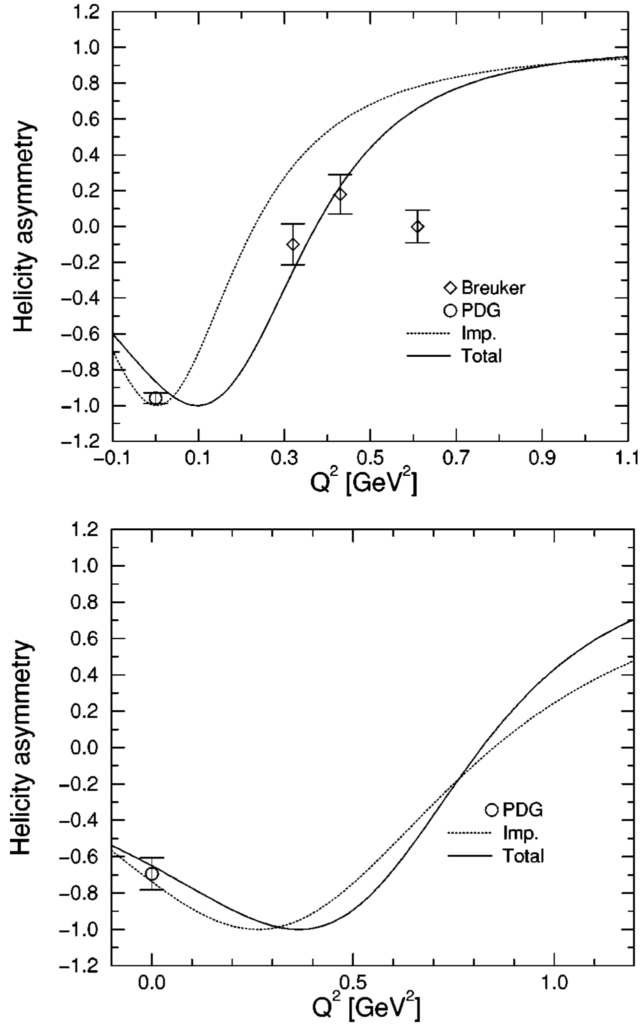

FIG. 13. Helicity asymmetry of the $\gamma N \to D_{13}(1520)$ transition as a function of the four-momentum transfer Q^2. Upper figure: proton, lower figure: neutron. The dotted curve (Imp.) is the impulse approximation result. The full curve (Total) includes the exchange currents. The experimental data are from Refs. [72] (Breuker) and [11] (PDG).

been used to describe the hadronic and electromagnetic structure of the nucleon. The new points are (i) the calculation of transverse and scalar helicity amplitudes for finite four-momentum transfers Q^2; and (ii) the inclusion of configuration mixing for the positive parity nucleon resonances. The helicity amplitudes are further decomposed into electromagnetic multipoles and connected to the $\gamma N \to N^*$ transition form factors. The main results can be summarized as follows.

The Coulomb and electric quadrupole transitions to the $P_{33}(1232)$ are dominated by the two-body exchange currents. This conclusion holds with and without the inclusion of configuration mixing. Due to the exchange currents we obtain a better agreement with experiment for the $C2/M1$ and $E2/M1$ ratios in the electroexcitation of the $\Delta(1232)$. The present theory shows that the electromagnetic quadrupole excitation of the Δ is predominantly an excitation of the $q\bar{q}$ cloud degrees of freedom effectively described by the two-body exchange currents. The valence quark core does not significantly contribute to this mode of excitation.

The long-standing problem of the underestimation of the $M1$ excitation of the Δ by some 30% persists. Exchange currents do not solve this problem. The Beg-Lee-Pais relation between the nucleon and $N \to \Delta$ transition magnetic moment remains intact after including two-body exchange currents. We find that the nucleon magnetic moments and the $N \to \Delta$ transition magnetic moment are tightly related in the quark model with exchange currents. It seems impossible to generate a 30% change in $\mu_{p\to\Delta^+}$ without simultaneously spoiling the quark model predictions for the nucleon *and* Δ^+ magnetic moments.

For the magnetic dipole transition to the $P_{11}(1440)$, the addition of two-body exchange currents improves the agreement with experiment at $Q^2=0$, while preserving the success of the single-quark transition model in correctly predicting the experimental ratio $A_{1/2}^{p}/A_{1/2}^{n} \approx -3/2$. On the other hand, the experimentally observed electroquenching of the Roper excitation at finite momentum transfers cannot be explained by adding exchange currents. This suggests that the Roper involves the excitation of additional degrees of freedom, beyond the valence quark and $q\bar{q}$ cloud considered in this work.

In the case of the electric dipole excitation of the $S_{11}(1535)$, the inclusion of two-body exchange currents considerably improves the agreement between theory and experiment. The discrepancy at $Q^2=0$ between the single quark transition model prediction and experiment largely disappears after including exchange currents. Problems remain for momentum transfers above 0.5 GeV^2, where the absolute value of the $A_{3/2}^{p}$ amplitude of the $D_{13}(1520)$ is underestimated.

In summary, exchange currents provide important contributions for nearly all observables. Their inclusion allows to extend the region of validity of the CQM: more observables can be simultaneously described. For example, the electromagnetic transition to excited nucleon states and the ground state charge radii can now be described with a single size parameter. Exchange currents must be included in the CQM before one can conclude that one has seen a failure of the constituent quark model description of baryon structure. Equally important is the observation that certain observables, which are dominated by two-body exchange currents are interrelated. It would be interesting to apply these concepts to other nucleon properties such as the electric and magnetic polarizabilities and the weak form factors of the nucleon [73].

ACKNOWLEDGMENTS

A.J.B. thanks the Nuclear Theory Group at the University of Salamanca for hospitality and financial support. This work was supported in part by Junta de Castillia y Leon under Contract No. SA73/98.

APPENDIX: HELICITY AND MULTIPOLE AMPLITUDES

In this appendix the scalar and transverse helicity amplitudes are given in terms of Coulomb, electric, and magnetic multipole amplitudes. We recall the definition of the transverse (A) and scalar (S) helicity amplitudes [8]:

$$A_\lambda(\mathbf{q}^2) = -e\sqrt{\frac{2\pi}{\omega}}\langle N^*, M_{J_f}=\lambda|\boldsymbol{\epsilon}_1\cdot\mathbf{j}(\mathbf{q})|N, M_{J_i}=\lambda-1\rangle, \tag{A1}$$

$$S_\lambda(\mathbf{q}^2) = e\sqrt{\frac{2\pi}{\omega}}\langle N^*, M_{J_f}=\lambda|\rho(\mathbf{q})|N, M_{J_i}=\lambda\rangle, \tag{A2}$$

where $q_\mu = (\omega, -\mathbf{q})$ is the photon four-momentum, and $\boldsymbol{\epsilon}_1 = -(\mathbf{e}_x + i\mathbf{e}_y)/\sqrt{2}$ is the photon polarization vector for right circularly polarized photons. The three-momentum transfer $\mathbf{q}$ points in the z direction (see Fig. 1). Here, N stands for the nucleon with total angular momentum $J_i = 1/2$ and N^* stands for the excited nucleon resonance with angular momentum J_f. In order to connect the helicity amplitudes with the e.m. multipole amplitudes we decompose the three-vector current density according to Ref. [74] in electric (T^E) and magnetic (T^M) multipole operators

$$\mathbf{j}_m(\mathbf{q}) = -\sqrt{2\pi}\sum_{J=1}^{\infty} i^J\sqrt{2J+1}[mT_m^{[M]J}(q) + T_m^{[E]J}(q)]. \tag{A3}$$

Here, $m = 0, \pm 1$ are the spherical components of the spatial current $\mathbf{j}$[3] and J stands for the total angular momentum of the photon. Similarly, we obtain for the zeroth component of the current density

$$\rho(\mathbf{q}) = \sqrt{4\pi}\sum_{J=0}^{\infty} i^J\sqrt{2J+1}\,T_0^{[C]J}(q), \tag{A4}$$

where $T^{[C]J}$ is the Coulomb multipole operator.

The electromagnetic multipole operators are defined in terms of the charge and current density as follows [75]:

$$T_M^{[C]J}(q) = \frac{(-i)^J}{4\pi}\int d\hat{\mathbf{q}}[Y^J(\hat{\mathbf{q}})\otimes\rho(\mathbf{q})]_M^J, \tag{A5}$$

$$T_M^{[M]J}(q) = \frac{(-i)^J}{4\pi}\int d\hat{\mathbf{q}}[Y^J(\hat{\mathbf{q}})\otimes\mathbf{j}(\mathbf{q})]_M^J, \tag{A6}$$

$$T_M^{[E]J}(q) = \sqrt{6}\sqrt{2J+1}(-1)^J\sum_{L=J\pm1}\sqrt{2L+1}\begin{pmatrix} J & 1 & L \\ 0 & 0 & 0\end{pmatrix} \times\begin{Bmatrix} J & 1 & L \\ 1 & J & 1\end{Bmatrix}\frac{(-i)^J}{4\pi}\int d\hat{\mathbf{q}}[Y^L(\hat{\mathbf{q}})\otimes\mathbf{j}(\mathbf{q})]_M^J. \tag{A7}$$

For the transverse and scalar helicity amplitudes we then obtain

$$A_\lambda(\mathbf{q}^2) = e\sqrt{\frac{2\pi}{\omega}}\sum_{J=1}^{\infty}\langle N^*, M_{J_f}=\lambda|\sqrt{2\pi}i^J\sqrt{2J+1}[T_1^{[M]J}(q) + T_1^{[E]J}(q)]|N, M_{J_i}=\lambda-1\rangle,$$

$$S_\lambda(\mathbf{q}^2) = e\sqrt{\frac{2\pi}{\omega}}\sum_{J=0}^{\infty}\langle N^*, M_{J_f}=\lambda|\sqrt{4\pi}i^J\sqrt{2J+1} \times T_0^{[C]J}(q)|N, M_{J_i}=\lambda\rangle. \tag{A8}$$

Due to the conservation of the total angular momentum, $\mathbf{J}_i + \mathbf{J} = \mathbf{J}_f$ and parity $\pi_i\pi_\gamma = \pi_f$ only a few transition multipoles contribute. For the positive parity excitations with $J_f = 1/2$ $M1$ and $C0$ radiation contributes. For the positive parity resonances with $J_f = 3/2$, such as the $\Delta(1232)$, only the $M1$, $E2$, and $C2$ multipoles are nonzero.

Using the Wigner-Eckart theorem [76], the helicity amplitudes for the positive parity resonances may be expressed in terms of reduced matrix elements of the multipole operators:

$\underline{J_f^\pi = \frac{1}{2}^+}$

$$A_{1/2}(\mathbf{q}^2) = -ie\frac{2\pi}{\sqrt{\omega}}\langle N^*||T^{M1}(q)||N\rangle, \tag{A9}$$

$$S_{1/2}(\mathbf{q}^2) = e\frac{2\pi}{\sqrt{\omega}}\langle N^*||T^{C0}(q)||N\rangle, \tag{A10}$$

$\underline{J_f^\pi = \frac{3}{2}^+}$

[3]We use $\mathbf{j}$ instead of $\mathbf{J}$ in this appendix in order to avoid confusion with the angular momentum J.

$$A_{1/2}(\mathbf{q}^2)=\frac{e}{\sqrt{\omega}}\big(\pi i\langle N^*||T^{M1}(q)||N\rangle + \sqrt{3}\pi\langle N^*||T^{E2}(q)||N\rangle\big), \tag{A11}$$

$$A_{3/2}(\mathbf{q}^2)=\frac{e}{\sqrt{\omega}}\big(\sqrt{3}\pi i\langle N^*||T^{M1}(q)||N\rangle - \pi\langle N^*||T^{E2}(q)||N\rangle\big), \tag{A12}$$

$$S_{1/2}(\mathbf{q}^2)=-\frac{2\pi e}{\sqrt{\omega}}\langle N^*||T^{C2}(q)||N\rangle. \tag{A13}$$

For the negative parity resonances with $J_f=1/2$, we obtain $C1$ and $E1$ contributions. The $J=3/2$ resonances with negative parity can, in addition be excited with $M2$ radiation.

$\underline{J_f^\pi=\tfrac{1}{2}^-}$

$$A_{1/2}(\mathbf{q}^2)=-ie\frac{2\pi}{\sqrt{\omega}}\langle N^*||T^{E1}(q)||N\rangle, \tag{A14}$$

$$S_{1/2}(\mathbf{q}^2)=ie\frac{2\pi}{\sqrt{\omega}}\langle N^*||T^{C1}(q)||N\rangle, \tag{A15}$$

$\underline{J_f^\pi=\tfrac{3}{2}^-}$

$$A_{1/2}(\mathbf{q}^2)=\frac{e}{\sqrt{\omega}}\big(\pi i\langle N^*||T^{E1}(q)||N\rangle + \sqrt{3}\pi\langle N^*||T^{M2}(q)||N\rangle\big), \tag{A16}$$

$$A_{3/2}(\mathbf{q}^2)=\frac{e}{\sqrt{\omega}}\big(\sqrt{3}\pi i\langle N^*||T^{E1}(q)||N\rangle - \pi\langle N^*||T^{M2}(q)||N\rangle\big), \tag{A17}$$

$$S_{1/2}(\mathbf{q}^2)=\frac{2ie\pi}{\sqrt{\omega}}\langle N^*||T^{C1}(q)||N\rangle. \tag{A18}$$

For the positive parity resonances we also express these in terms of e.m. transition form factors, defined as [75]

$$F^{C0}(\mathbf{q}^2)=\sqrt{4\pi}\left\langle N^*,M_{J_f}=\frac{1}{2}\middle|T^{C0}(q)\middle|N,M_{J_i}=\frac{1}{2}\right\rangle, \tag{A19}$$

$$F^{M1}(\mathbf{q}^2)=\sqrt{6\pi}\,\frac{2M_N}{i|\mathbf{q}|}\left\langle N^*,M_{J_f}=\frac{1}{2}\middle|T^{M1}(q)\middle|N,M_{J_i}=\frac{1}{2}\right\rangle, \tag{A20}$$

$$F^{E2}(\mathbf{q}^2)=\frac{12\sqrt{5\pi}}{\mathbf{q}^2}\left\langle N^*,M_{J_f}=\frac{1}{2}\middle|T^{E2}(q)\middle|N,M_{J_i}=\frac{1}{2}\right\rangle, \tag{A21}$$

$$F^{C2}(\mathbf{q}^2)=\frac{12\sqrt{5\pi}}{\mathbf{q}^2}\left\langle N^*,M_{J_f}=\frac{1}{2}\middle|T^{C2}(q)\middle|N,M_{J_i}=\frac{1}{2}\right\rangle. \tag{A22}$$

We then obtain the following relations between the e.m. form factors and the helicity amplitudes:

$\underline{J_f^\pi=\tfrac{1}{2}^+}$

$$A_{1/2}(\mathbf{q}^2)=\frac{e}{2M_N}\sqrt{\frac{\pi}{\omega}}2|\mathbf{q}|F^{M1}(\mathbf{q}^2), \tag{A23}$$

$$S_{1/2}(\mathbf{q}^2)=e\sqrt{\frac{2\pi}{\omega}}F^{C0}(\mathbf{q}^2), \tag{A24}$$

$\underline{J_f^\pi=\tfrac{3}{2}^+}$

$$A_{1/2}(\mathbf{q}^2)=-\frac{e}{2M_N}\sqrt{\frac{\pi}{\omega}}|\mathbf{q}|\left(F^{M1}(\mathbf{q}^2)-\frac{|\mathbf{q}|M_N}{\sqrt{6}}F^{E2}(\mathbf{q}^2)\right), \tag{A25}$$

$$A_{3/2}(\mathbf{q}^2)=-\frac{e}{2M_N}\sqrt{\frac{3\pi}{\omega}}|\mathbf{q}|\left(F^{M1}(\mathbf{q}^2)+\frac{|\mathbf{q}|M_N}{3\sqrt{6}}F^{E2}(\mathbf{q}^2)\right), \tag{A26}$$

$$S_{1/2}(\mathbf{q}^2)=-e\sqrt{\frac{2\pi}{\omega}}\frac{\mathbf{q}^2}{6}F^{C2}(\mathbf{q}^2). \tag{A27}$$

[1] Volker D. Burkert, Czech. J. Phys. **46**, 627 (1996).
[2] C. M. Becchi and G. Morpurgo, Phys. Lett. **17**, 352 (1965).
[3] L. A. Copley, G. Karl, and E. Obryk, Nucl. Phys. **B13**, 303 (1969).
[4] R. Koniuk and N. Isgur, Phys. Rev. D **21**, 1868 (1980).
[5] M. Giannini, Rep. Prog. Phys. **54**, 453 (1990).
[6] T. Kubota and K. Ohta, Phys. Lett. **65B**, 374 (1976).
[7] Frank E. Close and Zhenping Li, Phys. Rev. D **42**, 2194 (1990).
[8] W. Warns, H. Schröder, W. Pfeil, and H. Rollnik, Z. Phys. C **45**, 627 (1990).
[9] Simon Capstick, Phys. Rev. D **46**, 2864 (1992).
[10] S. Capstick and G. Karl, Phys. Rev. D **41**, 2767 (1990).
[11] Particle Data Group, C. Caso *et al.*, Eur. Phys. J. C **3**, 1 (1998).
[12] R. H. Dalitz and D. G. Sutherland, Phys. Rev. **146**, 1180 (1966).
[13] Zhenping Li, V. Burkert, and Zhujun Li, Phys. Rev. D **42**, 70 (1992).
[14] A. Buchmann, E. Hernández, and K. Yazaki, Phys. Lett. B **269**, 35 (1991); Nucl. Phys. **A569**, 661 (1994).
[15] A. J. Buchmann, E. Hernández, U. Meyer, and A. Faessler, Phys. Rev. C **58**, 2478 (1998); A. J. Buchmann, E. Hernández, and A. Faessler, *ibid.* **55**, 448 (1997).
[16] U. Meyer, A. J. Buchmann, and A. Faessler, Phys. Lett. B **408**,

19 (1997); A. J. Buchmann, U. Meyer, E. Hernández, and A. Faessler, Acta Phys. Pol. A **27**, 3161 (1996).
[17] G. Wagner, A. J. Buchmann, and A. Faessler, Phys. Rev. C **58**, 1745 (1998); **58**, 3666 (1998).
[18] A. J. Buchmann, Z. Naturforsch., A: Phys. Sci. **52a**, 877 (1997).
[19] E. Perazzi, M. Radici, and S. Boffi, Nucl. Phys. **A614**, 346 (1997).
[20] D. Robson, Nucl. Phys. **A560**, 389 (1993).
[21] A. J. Buchmann, Nucl. Phys. **A670**, 174c (2000).
[22] R. Beck *et al.*, Phys. Rev. Lett. **78**, 606 (1997).
[23] G. Blanpied *et al.*, Phys. Rev. Lett. **79**, 4337 (1997).
[24] The LEGS Collaboration, G. Blanpied *et al.*, Phys. Rev. C **64**, 025203 (2001).
[25] P. Bartsch, in *Proceedings of Baryons' 98*, Bonn, Germany, edited by D. W. Menze and B. Metsch (World Scientific, Singapore, 1999), p. 757.
[26] I. T. Obukhovsky and A. M. Kusainov, Phys. Lett. B **228**, 142 (1990).
[27] F. Fernández, A. Valcarce, U. Straub, and Amand Faessler, J. Phys. G **19**, 2013 (1993); A. Valcarce, A. J. Buchmann, A. Faessler, and F. Fernández, Phys. Rev. C **50**, 2246 (1994); **51**, 1480 (1995).
[28] A. de Rújula, H. Georgi, and S. L. Glashow, Phys. Rev. D **12**, 147 (1975).
[29] N. Isgur and G. Karl, Phys. Rev. D **18**, 4187 (1978); **19**, 2653 (1979); N. Isgur, G. Karl, and R. Koniuk, Phys. Rev. Lett. **41**, 1269 (1978).
[30] L. Ya. Glozman, W. Plessas, K. Varga, and R. F. Wagenbrunn, Phys. Rev. D **58**, 094030 (1998).
[31] S. Boffi, P. Demetriou, M. Radici, and R. F. Wagenbrunn, Phys. Rev. C **60**, 025206 (1999).
[32] N. Isgur, *Proceedings of Baryons' 98* (Ref. [25]), p. 1.
[33] X. Song, Phys. Rev. D **40**, 3655 (1989); Y. Wang and D. Lichtenberg, *ibid.* **42**, 2404 (1990).
[34] Zong-Ye Zhang, You-Wen Yu, Peng-Nian Shen, Xiao-Yan Shen, and Yu-Bin Dong, Nucl. Phys. **A561**, 595 (1993).
[35] A. J. Buchmann and R. F. Lebed, Phys. Rev. D **62**, 096005 (2000).
[36] G. Dillon and G. Morpurgo, Phys. Lett. B **448**, 107 (1999).
[37] U. Vogl and W. Weise, Prog. Part. Nucl. Phys. **27**, 195 (1991).
[38] F. Cardarelli, E. Pace, G. Salmè, and S. Simula, Phys. Lett. B **371**, 7 (1996); **397**, 13 (1997).
[39] R. Bijker, F. Iachello, and A. Leviatan, Ann. Phys. (N.Y.) **236**, 69 (1994).
[40] R. Sartor and F. Stancu, Phys. Rev. D **33**, 727 (1986).
[41] Frank E. Close and Zhengping Li, Phys. Rev. D **42**, 2194 (1990).
[42] A. Lubatsch and A. J. Buchmann (unpublished).
[43] G. Dillon and G. Morpurgo, hep-ph/0011202.
[44] A. J.Buchmann, in *Excited Nucleons and Hadronic Structure*, Proceedings of NSTAR 2000 Workshop, Newport News, VA, 2000, edited by V. Burkert, L. Elouadrhiri, J. J. Kelly, and R. C. Minehart (World Scientific, Singapore, 2001), p. 59.
[45] A. I. Machavariani, A. Faessler, and A. J. Buchmann, Nucl. Phys. **A646**, 231 (1999); D. Drechsel, M. Vanderhaeghen, M. M. Giannini, and E. Santopinto, Phys. Lett. B **484**, 236 (2000).
[46] S. Schadmand, Acta Phys. Pol. B **31**, 2431 (2000).
[47] Th. Wilbois, P. Wilhelm, and H. Arenhoevel, Phys. Rev. C **57**, 295 (1998).
[48] R. M. Davidson, N. C. Mukhopadhyay, M. S. Pierce, R. Arndt, I. I. Strakovsky, and R. L. Workman, Phys. Rev. C **59**, 1059 (1998); O. Hanstein, L. Tiator, and D. Drechsel, Phys. Lett. B **385**, 45 (1996); T. Sato and T.-S. H. Lee, Phys. Rev. C **54**, 2660 (1996); S. S. Kamalov and S. N. Yang, Phys. Rev. Lett. **83**, 4494 (1999).
[49] N. Isgur, G. Karl, and R. Koniuk, Phys. Rev. D **25**, 2394 (1982); S. S. Gershtein and G. V. Dzhikiya, Yad. Fiz. **34**, 1566 (1981) [Sov. J. Nucl. Phys. **34**, 872 (1982)].
[50] J. C. Alder *et al.*, Nucl. Phys. **B46**, 573 (1972).
[51] K. Baetzner *et al.*, Nucl. Phys. **B76**, 1 (1974).
[52] R. Siddle *et al.*, Nucl. Phys. **B35**, 93 (1971).
[53] C. Mertz *et al.*, Phys. Rev. Lett. **86**, 2963 (2001).
[54] Th. Popischil, Phys. Rev. Lett. **86**, 2959 (2001).
[55] R. Gothe, in *Excited Nucleons and Hadronic Structure*, Proceedings of NSTAR2000 Workshop, Newport News, VA, 2000, edited by V. Burkert, L. Elouadrhiri, J. J. Kelly, and R. C. Minehart (Ref. [44]), p. 31.
[56] Experimentalists usually define $C2/M1 = S_{1+}(\mathbf{q}^2)/M_{1+}(\mathbf{q}^2)$, and $E2/M1 = E_{1+}(\mathbf{q}^2)/M_{1+}(\mathbf{q}^2)$. For the relation between the pion production multipoles S_{1+}, E_{1+}, and M_{1+} and the helicity amplitudes $A_{1/2}$, $A_{3/2}$, and $S_{1/2}$, see Ref. [8].
[57] A. J. Buchmann and E. M. Henley, Phys. Rev. C **63**, 015202 (2001).
[58] P. Grabmayr and A. J. Buchmann, Phys. Rev. Lett. **86**, 2237 (2001).
[59] S. Galster *et al.*, Phys. Rev. D **5**, 519 (1972).
[60] I. G. Aznauryan and S. G. Stepanyan, Phys. Rev. D **59**, 054009 (1999).
[61] C. E. Carlson, Phys. Rev. D **34**, 2704 (1986); V. D. Burkert and L. Elouadrhiri, Phys. Rev. Lett. **75**, 3614 (1995).
[62] O. Krehl, C. Hanhart, S. Krewald, and J. Speth, Phys. Rev. C **62**, 025207 (2000).
[63] R. K. Bhaduri, B. K. Jennings, and J. C. Waddington, Phys. Rev. D **29**, 2051 (1983).
[64] Y. B. Dong *et al.*, Phys. Rev. C **60**, 035203 (1999).
[65] M. Aiello, M. Ferraris, M. M. Giannini, M. Pizzo, and E. Santopinto, Phys. Lett. B **387**, 215 (1996).
[66] M. Giannini (private communication).
[67] C. Gerhardt, Z. Phys. C **4**, 311 (1980).
[68] B. Krusche, Phys. Rev. Lett. **74**, 3736 (1995).
[69] M. Aiello, M. M. Giannini, and E. Santopinto, J. Phys. G **24**, 753 (1998).
[70] G. Karl, in *Proceedings of Baryons' 92*, New Haven, CT, 1992, edited by Moshe Gai (World Scientific, Singapore, 1993).
[71] R. Thompson *et al.*, Phys. Rev. Lett. **86**, 1702 (2001).
[72] H. Breuker *et al.*, Z. Phys. C **13**, 113 (1982); **17**, 121 (1983).
[73] D. Barquilla-Cano, A. J. Buchmann, and E. Hernández (work in progress).
[74] T. DeForest, Jr. and J. D. Walecka, Adv. Phys. **15**, 144 (1966).
[75] M. Gari and H. Hyuga, Nucl. Phys. **A264**, 409 (1976).
[76] I. Talmi and A. de Shalit, *Nuclear Shell Theory* (Academic, New York, 1963).